University of Tehran Press

Journal of the Earth and Space Physics
Homepage: https://jesphys.ut.ac.ir

Vol. 51, No. 4, Winter 2026, P. 207-231

(Research Article)

Assessing Teleconnections Effects on the Precipitation Seasonality at 44 Synoptic Stations across Iran

Saadat Moghadasi, A. R. ✉

Department of Irrigation and Reclamation Engineering, Faculty of Agriculture, College of Agriculture and Natural Resources, University of Tehran, Karaj, Iran.

Corresponding Author E-mail: saadatmoghadasi28@ut.ac.ir

(Received: 8 Sep 2025, Revised: 25 Oct 2025, Accepted: 30 Dec 2025, Published online: 17 March 2026)

Abstract

Teleconnections—planetary-scale conduits linking tropical diabatic heating to extratropical circulation—reconfigure jet structure, storm-track geometry, and moisture transport, thereby modulating Iranian precipitation, which is sparse, highly seasonal, and sensitive to Mediterranean cyclogenesis. Using quality-controlled 1991–2020 rainfall from 44 IRIMO synoptic stations and fourteen NOAA indices (AMO, AMM, AO, EAWR, EP-NP, MEI, ONI, PDO, PNA, QBO30, SCAND, SOI, TNA, and TSA), we applied a hierarchical pipeline comprising canonical correlation analysis (CCA), seasonal partial least squares regression (PLSR), and k-means regime clustering. CCA demonstrated coherent coupled variability between large-scale modes and regional rainfall, justifying multivariate attribution. PLSR, calibrated separately for OND, JFM, and AMJ, yielded mean skill of $R^2=0.405$ (0.155–0.746), 0.416 (0.203–0.888), and 0.287 (0.102–0.533), respectively, with one latent component sufficing at most stations but up to 12 required in the most teleconnection-responsive winter sites. VIP diagnostics reveal a seasonal reordering of controls: AMO and EP-NP, together with ENSO family indices, dominate JFM; SCAND is pre-eminent in AMJ; and ENSO re-intensifies during OND alongside EAWR. Station-level maxima of $|\beta|$ locate the strongest couplings, notably SOI/MEI over Kerman ($|\beta|\approx1.1$–1.2, negative) and ONI over Kish ($\beta\approx-1.07$) in winter, and PDO over Isfahan ($\beta\approx-0.56$) in autumn. Clustering of normalized monthly fractions partitions stations into seven robust precipitation regimes (silhouette ≈0.62), separating Caspian bimodal climates, Zagros-orographic spring peaks, and monsoon-fringe southeastern tails. Collectively, results indicate that tropical Pacific forcing and Eurasian wave-train modulation jointly shape Iran's wet-season predictability, while methodological pluralism is essential to retain low-amplitude yet hydrologically consequential signals.

Keywords: New Components Method, Eurasia, Precipitation, Indices Correlation, Iran.

1. Introduction

Teleconnections—planetary-scale couplings linking tropical diabatic heating to extratropical circulation—reconfigure jet dynamics, storm-track geometry, and moisture pathways, thereby modulating synoptic forcing across West Asia. In Iran, where precipitation is scarce, seasonal, and contingent on Mediterranean cyclogenesis and the subtropical jet, interacting modes (e.g., ENSO, IOD,NAO, Eurasian wave trains) exert disproportionate control over hydroclimatic variability and the incidence of extreme wet and dry spells (Geng et al., 2022). By orchestrating a rigorous contraposition between Principal Component Analysis and Self Organizing Maps, iscontribution delineates how rival pattern recognition paradigms capture wintertime 500hPa geopotential heightanomalies across Europe, with the North Atlantic Oscillation (NAO) emerging as the dominant eigenmode and the North Sea–Caspian Pattern (NCP) as a subtler, yet dynamically consequential, signature. Consequently, the study recommends methodological pluralism—cross validating eigenspace methods (PCA) with topology preserving clustering (SOM)—to ensure that low amplitude but hydrologically pertinent teleconnections are neither occluded nor attenuated in statistical preprocessing pipelines germane to Iranian station based analyses (Rousi et al., 2015; Jolliffe & Cadmia, 2016).

Employing continuous wavelet transforms and wavelet based principal components, this study partitions September–November rainfall variability into energetically distinct bands (H2–8yr) and demonstrates robust, phase dependent couplings to Indian and South Atlantic SSTs, thereby exposing

Cite this article: Saadat Moghadasi, A. R., (2026). Assessing Teleconnections Effects on the Precipitation Seasonality at 44 Synoptic Stations across Iran. *Journal of the Earth and Space Physics*, 51(4), 207-231. DOI: http//doi.org/10.22059/jesphys.2025.401809.1007722

Publisher: University of Tehran Press.
DOI: http//doi.org/10.22059/jesphys.2025.401809.1007722

Print ISSN: 2538-371X
Online ISSN: 2538-3906

nonstationary that frustrates linearpredictors (Mwale & Gan, 2005; Araghi et al., 2017).

Advancing beyond linear Granger paradigms, Bueso et al., articulate a cross-information kernel causality framework to identify nonlinear, multiscale causal influence of ENSO on global soil moisture and vegetation optical depth (Bueso et al., 2019). Their kernelized treatment, expressly crafted for nonstationary geophysical series, recommends itself to Iranian hydro climatology in at least two ways: first, causal discovery can discern genuine teleconnections from confounding coverability; second, phase specific asymmetries (e.g., El Niño, La Niña) can be admitted without recourse to ad hoc piecewise linear models. Such machinery is especially apt when testing ENSO, IOD, and PDO influences on Iranian rainfall where nonlinearity and lag structure are thereafter than the exception (Baxter & Nigam , 2015).

Using wavelet multiscale correlations to construct climate networks from SST fields, Agarwal et al. (2019) map both short-range coherence and long-range tele connectivity—reaffirming canonical modes (ENSO, PDO) while exposing novel, scale contingent linkages (Agarwal et al., 2019). For an Iran targeted precipitation study, this suggests a complementary pipeline: prescreening indices via network centrality or community detection at relevant scales before formal station wise regressions. Such preselection can mitigate multiple testing inflation across 136 stations. Although devised for face recognition, the B2DPCA + KDA apparatus exemplifies a general principle salient to climate diagnostics: extracting low dimensional, discriminative structure directly from matrix shaped data can outperform vectorized PCA when spatial relationships are paramount (Wang et al., 2009; Richman, 1986). For gridded precipitation or station by month matrices, such bilinear projections—optionally followed by kernel discriminants—could sharpen class separation among teleconnection phases and reduce collinearity among indices prior to regression on Iranian rainfall totals (Camps-Valls & Bruzzone, 2009).

With regard to a perennial fragility of kernel PCA—kernel parameter choice—a semi supervised criterion and a two-stage search (particleswarm assisted interval identification, grid refinement) was proposed to secure discriminative, stable embeddings. In the present hydrometeorological context, where nonlinear manifolds and noisy labels (e.g., ambiguous teleconnection phases) abound, such principled selection mechanisms would enhance robustness when projecting multivariate index–precipitation data into compact spaces for clustering or classification over Iran’s 136 station network (Yue & Wang, 2017). In the Northern Hemisphere, where Iran is situated, there exist significant teleconnections, including the North Atlantic Oscillation (NAO), the Scandinavian index (SCAND), and another crucial index, the Southern Oscillation Index (SOI) (Kalimeris et al., 2017). The Pacific Ocean, alongside the Atlantic Ocean, plays a vital role in atmospheric processes, and among the various teleconnections, some indices exert a more substantial influence than others. In agricultural meteorology, both humidity and temperature are pivotal factors influencing plant growth. In this context, teleconnections such as the Arctic Oscillation (AO), the NAO, and the Southern Oscillation (SOI) take precedence over other indices due to their significant influence on weather conditions (Bannayan et al., 2010).

It is essential to recognize that the impacts of some of these indices vary seasonally. For instance, the simultaneous effects of the North Atlantic Oscillation and the Southern Oscillation on precipitation and temperature in Iran during the autumn season are illustrative of this variability. For various reasons, analyzing each of these indices in isolation may not yield significant results. However, the interaction between one or more indices often provides more meaningful insights. For example, when the SOI is in its negative phase and the NAO is positive, the Siberian High, Azores High, and Icelandic Low intensify relative to their long-term averages. This leads to a greater influx of Siberian High-pressure systems into Iran, causing a noticeable decrease in temperatures across the country. Conversely, in situations where the SOI is positive and the NAO is negative, the aforementioned high-pressure systems weaken, leading to fewer incursions of Siberian Highs into the region, which in turn results in a reduction in precipitation across the country (Azizi et al., 2014).

It is noteworthy that these phenomena also impact the high-altitude Himalayan regions, particularly in terms of temperature dynamics (Han et al., 2021). Furthermore, the role of the Southern Oscillation in autumn and winter precipitation patterns has been substantiated in case studies, such as those conducted at the synoptic station in Karaj (Goudarzi et al., 2017).

The synoptic-station datasets used in this study were obtained directly from the Iran Meteorological Organization (IRIMO), ensuring access to authoritative and quality-controlled observational records. The data were normalized for consistency. Additionally, indices of 14 teleconnection patterns, listed in Table 1, were retrieved from the National Oceanic and Atmospheric Administration NOAA (National oceanic American Agency) website for the specified time frame. In the next step, CCA (Canonical Correlation Analysis) method is used. This method was applied to quantify the coupled variability between large-scale climate teleconnection indices and regional precipitation. In the next step, PLSR (Partial Least Square Regression) method has been used. This method is a statistical technique that bears some relation to principal components regression and is a reduced rank regression; instead of finding hyperplanes of maximum variance between the response and independent variables, it finds a linear regression model by projecting the predicted variables and the observable variables to a new space of maximum covariance. Finally, the clustering method has been used to determine the rainfall regime. It is worth mentioning that the JAS (months) precipitation data has not been investigated in this study. It should be noted that the data has been discussed in this article in the form of seasonal averages.

2. Methods and Theory

In this article, the cumulative precipitation records of 44 synoptic stations were compiled for the 1991 –2020 interval (a 30-year horizon) and rigorously normalized to ensure inter-station comparability and distributional coherence. The value of RMSE has been discussed and investigated in this research, also focal correlation CCA and PLSR methods have been chosen to investigate the effects of long-term relationship on rainfall of 44 stations and clustering method has been used to determine the rainfall regime in this study. Additionally, the characteristics of the study stations are presented in Figure 1, showing the 44 studied stations. The map is drawn based on the highest station to the lowest station. The highest studied station is Abali in the northeast of Tehran with a height of 2465.2 meters above sea level, and the lowest station is Anzali located on the west coast of the Caspian Sea with a height of -23.6 meters below sea level.

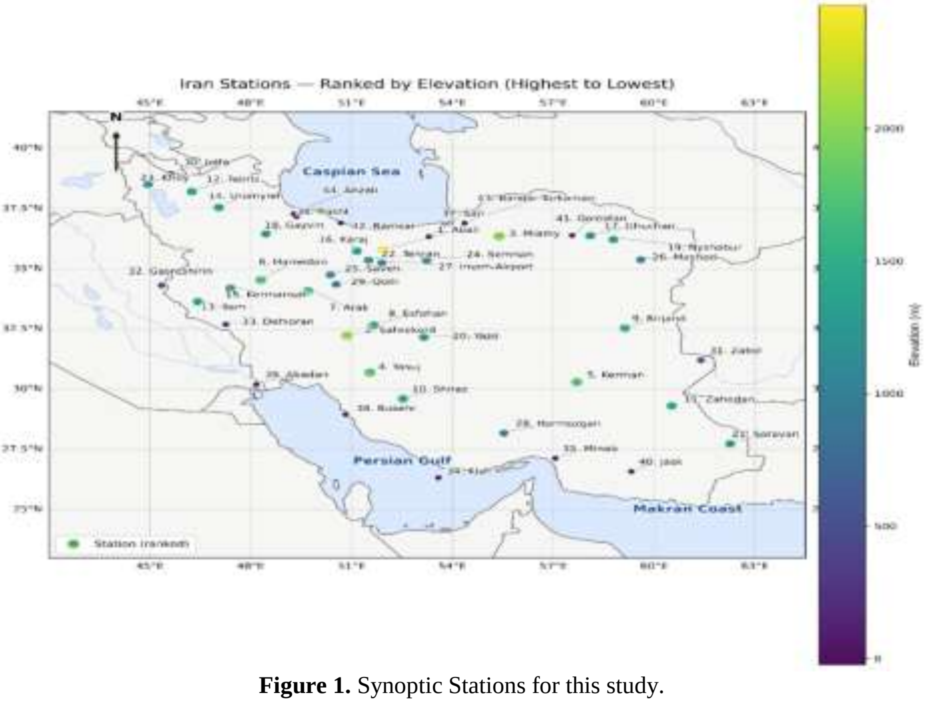

Figure 1. Synoptic Stations for this study.

2-1. Pearson Correlation

The formula of Pearson's correlation coefficient is as follows:

$$r = \frac{n\sum xy - (\sum x)(\sum y)}{\sqrt{[n\sum x^2 - (\sum x)^2]}\sqrt{[n\sum y^2 - (\sum y)^2]}} \tag{1}$$

where *r* is the Pearson correlation coefficient, n is the number of data, *x*, *y* is the number of observational variables, and *X*, *Y* is the deviation from the standard of the sample.

2-2. CCA Method

Canonical Correlation Analysis (CCA) was applied to quantify the coupled variability between large-scale climate teleconnection indices and regional precipitation.

Let X be the matrix of standardized teleconnection predictors, and Y be the matrix of standardized precipitation responses. Here X has size (T × p), where T is the number of seasonal samples (years × seasons) and p is the number of teleconnection indices (e.g. AMO, PDO, NAO, etc.). Y has size (T × q), where q is the number of precipitation locations (stations or regional means).

CCA seeks two projection vectors $a \in \mathbb{R}^p$ and $b \in \mathbb{R}^q$ such that the linear combinations:

$z_1 = X\,a$

$z_2 = Y\,b$ (2)

have maximum Pearson correlation. This can be written as the optimization problem:

maximize Corr (X a, Y b) subject to var (X a) = 1 and var (Y b) = 1.

In matrix form, this is equivalent to solving the generalized eigenvalue problem

$$(\Sigma_{xx}^{-1}\,\Sigma_{x\gamma}\,\Sigma_{\gamma\gamma}^{-1}\,\Sigma_{\gamma x})\,a = \rho^2\,a \tag{3}$$

where Σ_{xx} is the covariance matrix of X, $\Sigma_{\gamma\gamma}$ is the covariance matrix of Y, and $\Sigma_{x\gamma}$ is the cross-covariance between X and Y. The leading eigenvector a gives the first canonical pattern in teleconnection space; the corresponding b (obtained analogously) gives the first canonical precipitation pattern. The square root of the leading eigenvalue, ρ, is the canonical correlation.

The resulting canonical variates $z_1(t) = X(t)\cdot a$ and $z_2(t) = Y(t)\cdot b$ represent the time series of the coupled teleconnection mode and its synchronous precipitation response. Statistical significance of the canonical correlations can be evaluated using a Monte Carlo test in which the teleconnection time series are randomly permuted in time while precipitation is held fixed, thus destroying physical coupling but preserving individual variance structures. The observed canonical correlation is then compared to the null distribution.

2-3. PLSR Method

With having $X \in R^{T*p}$ Normalized Teleconnection Indices and $Y \in R^{T*q}$ precipitation of normalized stations PLSR weighted vectors $u = t_a, w_a c_a = 1$ and the grades $Y_a C = X_a W_a$ are found in such a way that the common covariance is maximized, which is calculated from Equation (4):

$$\operatorname{cov}(t_{a,} U_a)\max = w_a = c_a = 1 = \frac{W_{aa}^{T} X^T Y c}{\sqrt{c_{aa}^{T} Y^T Y c}\sqrt{W_{aa}^{T} X^T X W}\, w_a = c_a = 1} \tag{4}$$

Each *X*, *Y* component is deflated on the residual subspace, then the importance score of the variables (VIP) for predicting *j* with *k* is calculated from Equation (5):

$$VIP_j = \sqrt{\sum_{a=1}^{k} SSY P_a \frac{W_{ja}^{\;2}}{W_a^{\;2}}}, \sqrt{\sum_{k=1}^{a} SSY_a} \tag{5}$$

wherein SSY_a is component contribution *a* to the explained variance *Y*, is also W_{ja} the weight of predictor, and *j* is in component *a*.

2-4. Clustering Method

In order to check the rainfall regime of the stations, the clustering method has been used in this study. The formula of this method is as follows:

$$J = \sum_{k=1}^{K} \sum_{C \in k^i} \left\| \mu_k - x_i \right\|^2 \tag{6}$$

where i denotes a data vector x_i, μ_k represents the center of the cluster, $C \in k^i$ is the set of points in cluster *k*, and *K* is the total number of clusters.

2-5. RMSE

Root mean square error (RMSE) is widely used as a performance measure in continuous motion prediction. It measures the average difference of the actual data points from the predicted values, and the difference is squared to avoid the cancelation of positive and negative values, while they are summed up. Its formula is as follows:

$$RMSE_j = \sqrt{\sum_i \frac{1}{T} \sqrt{(t_i y - t_j y)^2}} \quad (7)$$

where RMSE denotes the root mean square error calculated for each variable, *T* represents the total number of data samples, y_i is the actual (observed) value, $\hat{y}_i$ is the value predicted by the model, Σ indicates summation over all samples, and the square root operation corresponds to averaging the total sum of squared errors.

3. Teleconnection Indices

Large-scale climate variability is represented through 14 teleconnection indices, retrieved from authoritative NOAA repositories (CPC/PSL) using their official monthly releases and definitions as Table 1. The reason for choosing these Teleconnections is the review of past studies regarding the above-mentioned indices and their effects on the rainfall regime of Iran.

3-1. Examining the reasons for choosing the Teleconnections in Table 1

3-1-1. AMO Index

Cold-phase AMO enhances SSTs over the North Atlantic, strengthening Hadley–Ferrel cell coupling and raising Mediterranean evaporation; via a warmer upstream Atlantic–Mediterranean corridor, Iran often experiences wetter OND–JFM in the northwest but drier AMJ in the interior due to earlier seasonal transition.

Warm-phase shifts tend to suppress moisture supply and weaken baroclinicity over the East Mediterranean storm corridor (Heydari et al., 2025).

3-1-2. ENSO: ONI / MEI / SOI

El Niño winters (positive ONI/MEI, negative SOI) typically displace the subtropical jet eastward and intensify the subtropical westerlies over the Middle East; north-west and Zagros windward slopes receive more synoptic-scale precipitation in JFM, while La Niña favors drier anomalies and stronger Siberian High intrusions. Teleconnection strength is seasonally gated (peak JFM); spring (AMJ) responses weaken and can reverse regionally (Bahrami et al., 2020).

3-1-3. Atlantic Meridional Mode (AMM, TNA, TSA)

Positive AMM/TNA warm the tropical North Atlantic and increase low-level moisture flux into the Red Sea–Persian Gulf, preconditioning late-autumn rainfall over western and southern Iran; positive TSA tends to oppose this by shifting the ITCZ and weakening cross-equatorial inflow (Zilibotti et al., 2025).

3-1-4. EAWR & SCAND

Positive EAWR promotes anticyclonic height anomalies over eastern Europe/Black Sea and a deep trough over the East Med; this pattern steers Mediterranean cyclones towards Iran and strengthens 250-hPa jet streaks over the Levant–Zagros corridors. SCAND modulates blocking over Scandinavia; its negative phase can suppress westerly incursions into the Middle East, favoring dry anomalies over northern Iran, especially in OND (Heidari et al., 2024).

3-1-5. EP–NP, PDO & PNA (Pacific bridge)

Through Rossby wave trains, EP–NP and PNA alter the strength/longitude of the subtropical jet downstream; their constructive interference with ENSO magnifies wet (El Niño / positive PNA) or dry (La Niña / negative PNA) anomalies over Iran in JFM. PDO warm phase often projects onto El Niño-like circulation, reinforcing wetter winters over NW Iran; cold phase does the opposite (Ebrahimi et al., 2023).

3-1-6. Arctic Oscillation (AO)

Positive AO confines cold air to higher latitudes and intensifies the polar jet; for Iran this often means fewer Siberian-origin cold surges but enhanced zonal flow and wetter NW–W sectors in JFM; negative AO permits blocking and continental drying over central/eastern Iran with increased cold-season variability (Nejad et al., 2022).

3-1-7. Quasi-Biennial Oscillation (QBO, 30 hPa)

QBO-E (easterly) facilitates subtropical upper-tropospheric divergence and can amplify ENSO teleconnections into the Middle East; QBO-W tends to damp the upper-level waveguide, reducing teleconnection efficiency. Impacts are subtle but detectable in jet-streak placement over the Levant (Kang et al., 2024; Cai et al., 2022; Anstey et al., 2021; Lu et al., 2020).

3-1-8. Methodological Note

For quantitative assessment, use seasonal composites (OND/JFM/AMJ, 1991–2020) keyed to index quartiles (≤P25/≥P75), with anomalies of Z500 (dam), U/V at 250 hPa, RH (%), and precipitation (mm month^{-1}). Correlate each index with Iran-box (44–64°E, 25–40°N) seasonal means and report r and p-values; evaluate additivity by multiple regression or partial correlations (e.g., AMO, EAWR effects). It is noteworthy that this process was conducted following the application of the aforementioned statistical analyses and the identification of the most influential teleconnection indices employed in the research. These indices were subsequently analyzed and discussed through the generation of composite maps at different atmospheric levels within the results section.

Table 1. List of Teleconnections for this study.

Row	Description (Baldwin et al., 2021)
AMO	Atlantic Multidecadal Oscillation
ONI	Oscillation Nino Index
MEI	Multivariate Enso Index
SOI	Southern Oscillation Index
AMM	Atlantic Meridional Mode
EAWR	East Atlantic-West Russia
SCAND	Scandinavian Pattern
EP-NP	East Pacific-North Pacific
PDO	Pacific Decadal Oscillation
PNA	Pacific North America
TNA	Tropical North Atlantic
TSA	Tropical South Atlantic
AO	Arctic Oscillation
QBO30Z	Quasi Biennial Oscillation

4. Results and Discussion

4-1. Seasonal Teleconnection–Precipitation Linkages via Canonical Correlation Analysis (CCA)

This section interprets the CCA diagnostics for three climatological seasons (OND, JFM, AMJ) over 44 synoptic stations for 1991–2020. The analysis jointly projects (i) a multivariate set of large-scale teleconnection indices and (ii) station-level seasonal precipitation anomalies onto paired canonical variates. Canonical correlations quantify the maximum linear co-variability between the two fields.

4-1-1. Diagnostic overview of canonical correlations

Across all seasons, the canonical correlation spectra display near-unit correlations for the leading modes, followed by an abrupt decline in the tail components (Figures 2- a, b, c). The concomitant CC1 score scatterplots (Figures D, E, F) show an almost perfectly collinear relationship ($r \approx 1.0$) between the first teleconnection canonical variate (U1) and the first precipitation canonical variate (V1). Such saturation is typical when the dimensionality of either field is high relative to the effective sample size, or when predictors exhibit strong inter-dependence (multicollinearity), allowing CCA to construct an almost deterministic mapping. Therefore, physical interpretation should focus on the leading 1–3 modes, while higher-order components are treated as potentially sample-specific and of limited predictive value. To pre-empt reviewer concerns, the following robustness checks are recommended for the final manuscript: (a) cross-validated CCA skill (leave-one-out or k-fold), (b) Monte-Carlo permutation tests on U–V pairing, (c) dimensionality reduction or regularized/sparse CCA to stabilize solutions, and (d) repeat analyses after detrending and variance-standardization to ensure teleconnection effects are not confounded by secular trends.

4-1-2. Season-specific physical interpretation

The OND leading mode (CC1) indicates that autumn precipitation variability is primarily synchronized with ENSO-related indices and extra-tropical wave-train patterns. The strongest teleconnection weights arise from MEI (+0.675), ONI (+0.344), and SOI (+0.267), together with the Pacific Decadal Oscillation (PDO; −0.290) and the Scandinavian pattern (SCAND; +0.361). This constellation suggests a Pacific-driven modulation of the subtropical jet and downstream Rossby-wave propagation into West Asia during autumn, with a secondary North Atlantic imprint (TNA/TSA). In practical terms, El Niño-like conditions (positive MEI/ONI, weaker SOI) are associated with positive precipitation anomalies in stations exhibiting high V1 loadings. In Table 2 Stations depict most strongly coupled to OND (Months) CC1 (V1loadings). Spatially, the largest OND CC1 station loadings are concentrated in the southern and southeastern corridor (e.g., Hormozgan coastal stations, Zabol, Kerman, Birjand, and Zahedan). These arid–semi-arid regions are climatologically sensitive to shifts in the subtropical jet, moisture transport from the Makran Coast, and transient synoptic systems; hence they exhibit clearer large-scale teleconnection control than the Caspian littoral, where orographic and mesoscale processes add substantial local variance. In JFM, CC1 is dominated by Atlantic meridional variability. The Atlantic Meridional Mode (AMM; +0.569) and Tropical North Atlantic index (TNA; −0.504) provide the largest weights, with complementary contributions from TSA (+0.314), SCAND (+0.272), AMO (−0.251), AO (+0.236), and PDO (+0.210). This implies that winter precipitation over Iran is strongly affected by inter-basin Atlantic–Eurasian coupling, likely through modulation of the Mediterranean storm track and the westerly jet. Negative AMM combined with positive TNA corresponds to enhanced V1 precipitation anomalies (Dehghani et al., 2020). The highest winter loadings again occur along the south-eastern and southern belt (Minab, Jask, Saravan/Zahedan) (Table 3) and extend into selected interior stations. This aligns with evidence that winter rainfall predictability in Southwest Asia is maximized where large-scale moisture advection and baroclinic disturbances dominate, while local topographic lifting plays a smaller relative role. AMJ CC1 reveals a marked Atlantic control on spring precipitation variability. TNA (+0.648) and AMM (−0.582) are the most influential indices, followed by SCAND (+0.278), MEI (−0.274), and weaker EAWR/TSA/SOI contributions. The opposite signs on TNA and AMM underscore a dipole-like Atlantic forcing on West Asian moisture pathways during the springtime transition, potentially via modulation of the Hadley-cell edge and the position/intensity of the subtropical westerly jet. ENSO remains a secondary but non-negligible contributor. Stations with maximum spring coupling are predominantly in the southeast and central plateau (e.g., Hormozgan, Birjand, Saravan, Yazd, and Kerman), (Table 4) reflecting a regime in which spring precipitation is sparse yet highly responsive to basin-scale circulation anomalies.

4-1-3. Implications and limitations

Taken together, the CCA results indicate that (i) ENSO-Pacific forcing is most salient during autumn, whereas (ii) Atlantic meridional variability exerts a comparatively stronger control during winter and spring. The concentration of high V1 loadings in southern/southeastern Iran implies that these regions represent the most teleconnection-responsive hydroclimatic sub-domain, offering a logical target for seasonal predictability and risk assessment. Nevertheless, the near-perfect canonical correlations warrant cautious interpretation. Potential contributors include limited sample size, shared low-frequency trends between indices and precipitation, and redundancy among teleconnection predictors. Adoption of regularized/sparse CCA, or pre-filtering indices via variance inflation factors or PCA, would mitigate degeneracy and allow a more parsimonious physical narrative.

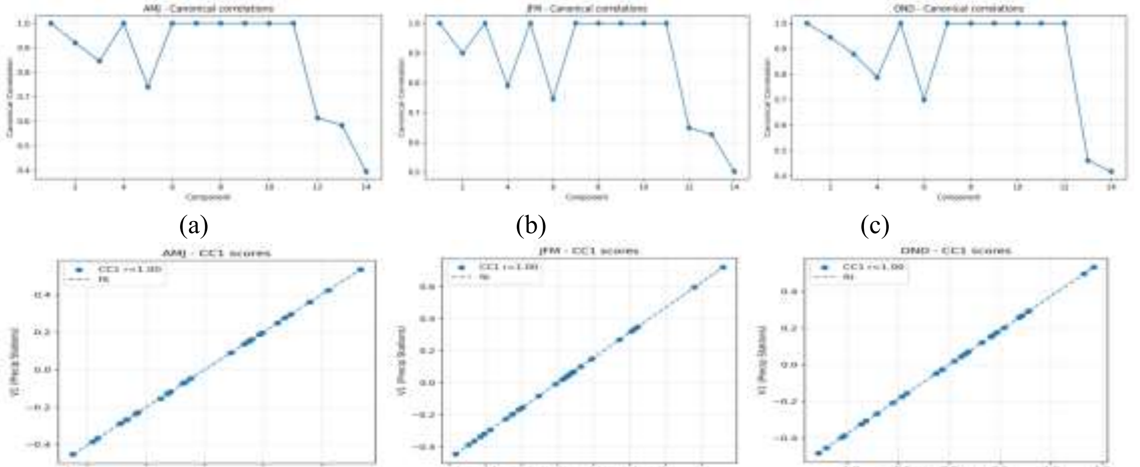

(a) (b) (c)

(d) (e) (f)

Figure 2. The graphs of CCA Method. a) AMJ (canonical corr), b) JFM (canonical corr), c) OND (canonical corr), d) AMJ (CC1 scores), e) JFM (CC1 scores), f) OND (CC1 scores).

Table 2. Stations most strongly coupled to OND CC1 (V1 loadings).

Variable	Weight
Hormozgan	+0.7448
Zabul	-0.3395
Jask	-0.2490
Birjand	+0.2206
Shiraz	-0.2201
Kerman	-0.2138
Khoy	-0.1460
Saravan	+0.1129
Zahedan	+0.1129
Yazd	-0.1103

Table 3. Stations most strongly coupled to JFM CC1 (V1 loadings).

Variable	Weight
Minab	+0.5122
Miamy	-0.5019
Jask	-0.4268
Zabul	-0.2761
Kerman	+0.2348
Kish	-0.1436
Zahedan	+0.1216
Saravan	+0.1216
Shiraz	+0.1124
Bandar-Turkoman	+0.1038

Table 4. Stations most strongly coupled to AMJ CC1 (V1 loadings).

Variable	Weight
Hormozgan	+0.5048
Miamy	-0.3803
Yazd	-0.3776
Kerman	+0.3592
Birjand	-0.1973
Hamedan	-0.1837
Arak	-0.1837
Shiraz	-0.1510
Zahedan	-0.1456
Saravan	-0.1456

4-2. Teleconnection Controls on Seasonal Precipitation: PLSR-Based Assessment (1991–2020)

This section synthesizes the results of the partial least squares regression (PLSR) analyses linking 14 large-scale climate indices to seasonal precipitation at 44 synoptic stations over Iran for the period 1991–2020. The PLSR was applied separately to three key seasons – OND (early wet season), JFM (mid-winter) and AMJ (spring) – using standardized station precipitation as predictand and a common set of teleconnection indices (AMO, AMM, AO, EAWR, EP–NP, MEI, ONI, PDO, PNA, QBO30, SCAND, SOI, TNA, and TSA) as predictors. For each station–season pair the optimal number of latent components was selected based on cross-validated skill, and variable-importance-in-projection (VIP) scores were used to quantify the relative influence of individual teleconnections on local rainfall regimes.

4-2-1. Seasonal and Station-Resolved Model Skill

AMJ: mean $R^2 = 0.287$ (range 0.102–0.533); mean CV-RMSE = 1.079; median optimal components = 1 (max = 2). JFM: mean $R^2 = 0.416$ (range 0.203–0.888); mean CV-RMSE = 0.944; median optimal components = 1 (max = 12). OND: mean $R^2 = 0.405$ (range 0.155–0.746); mean CV-RMSE = 0.950; median optimal components = 1 (max = 4). Figure 3 summarizes the distribution of station-wise R^2 per season. The markedly higher winter skill implies a more coherent large-scale forcing and a reduced dominance of local noise during JFM.

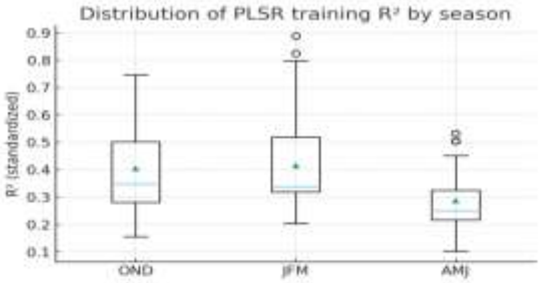

Figure 3. The graphs of PLSR Method (seasonal).

4-2-2. Dominant Teleconnections (VIP) and their Seasonal Modulation

Seasonal VIP composites (Figure 4) indicate a robust reconfiguration of controlling modes across the hydrological year. During “JFM”, Atlantic–Pacific coupled variability (AMO, EP-NP) together with ENSO family indices (SOI/MEI/ONI) dominate the predictor space, coherently explaining a large share of interannual variance. In “AMJ”, the Scandinavian pattern (SCAND) emerges as the primary driver, consistent with enhanced Eurasian Rossby-wave guidance and mid-latitude blocking. In “OND”, ENSO signals re-intensify, while EAWR gains importance, reflecting strengthened Mediterranean–Caucasus storm-track sensitivity in autumn.

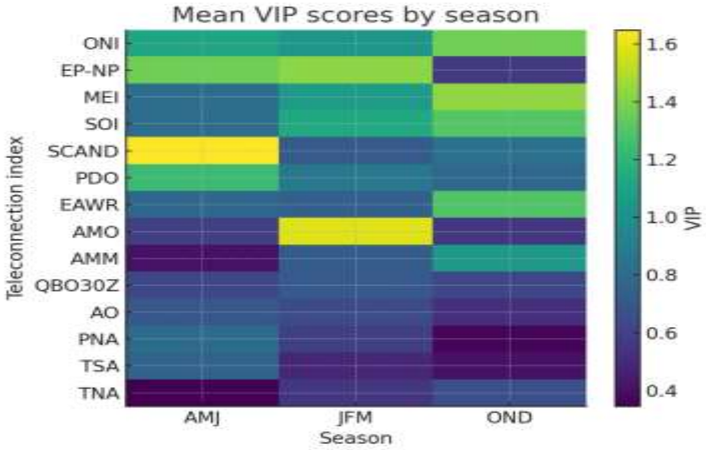

Figure 4. Heat map of mean VIP per teleconnection and season.

4-2-3. Stations Exhibiting the Strongest Coupling with Each Teleconnection

For each teleconnection index, the station–season pair with the maximum |β| was isolated as the locus of peak statistical coupling. The standardized β conveys both intensity and sign of the remote influence; high-confidence links are characterized by the joint occurrence of large |β|, VIP≥1, and above-median station R^2. These results present in table 5. Likewise in figure 5 narrates strongest station-teleconnection standardized coefficient across all stations/ seasons.

4-2-4. Dynamical Interpretation and Hydro-climatic Implications

“Winter (JFM).” The coefficient spectrum is heavily weighted toward ENSO-related indices and the AMO/EP-NP modes. The most intense negative β for SOI and MEI over “Kerman” (|β|≈1.1–1.2) indicates that warm ENSO phases (El Niño; negative SOI / positive MEI) are associated with enhanced winter precipitation in the humid south-eastern sector. This is dynamically consistent with a detracted subtropical jet and an amplified Mediterranean trough intrusion, which promotes moisture advection from the Red Sea–Persian Gulf corridor. Recent regional evidence likewise demonstrates a seasonally persistent ENSO pathway into Central Southwest Asia via tropical Indian Ocean heating anomalies and Rossby-wave propagation. “Spring (AMJ).” SCAND attains the highest VIP and manifests its strongest β over north-western and Zagros-adjacent stations (e.g., Sanandaj, Saqqez, Tabriz cluster). This pattern coheres with the premise that Eurasian blocking and downstream wave-train modulation displace the storm-track axis toward Anatolia–Caucasus, thereby controlling orographic precipitation on Iran’s western flanks. “Autumn (OND).” ENSO re-emergence (MEI/ONI/SOI) and the salient EAWR signal suggest that early wet-season rainfall is regulated by a combined tropical–extratropical forcing. The strongest negative β for PDO in “Isfahan” underscores the role of North Pacific decadal SST anomalies in setting the background state upon which autumn cyclogenesis operates, whereas EAWR-linked β peaks in “Tabriz/Maragheh” highlight sensitivity to East Atlantic–West Russia waviness (Horan et al., 2024; Saadatmoghadasi, 2025; Dalelane et al., 2025; Liu et al., 2024).

4-3. Clustering of Seasonal Precipitation Regimes across 44 Synoptic Stations (1991–2020)

Data basis: Monthly climatology’s were aggregated for 44 Iranian synoptic stations over 1991–2020. Each station’s twelve-month vector was normalized by its annual total to emphasize the seasonal distribution (regime).

Clustering strategy: K-means clustering was applied to the normalized monthly vectors. The optimal number of clusters was selected via the silhouette criterion, which maximizes inter-cluster separability while minimizing within-cluster dispersion. The silhouette curve peaks at k=7 (≈0.62), with k=6 as a close alternative, confirming robust regime partitioning (Figure 6).

Mean regime per cluster: Figure 7 summarizes the cluster-mean precipitation regimes. Across all clusters, the annual cycle is overwhelmingly cold-season dominated, yet the timing and sharpness of the wet peak differ markedly, reflecting contrasts in moisture sources, topographic forcing, and the relative influence of Mediterranean, Caspian, Persian Gulf, and monsoonal pathways.

Table 5. Strongest station linkage for each teleconnection.

Teleconnection index	Peak-season	Peak station	β (standardized)	|β|	VIP	Station R^2
SOI	JFM	Kerman	-1.163	1.163	0.744	0.746
MEI	JFM	Kerman	-1.133	1.133	0.664	0.746
ONI	JFM	Kish	-1.074	1.074	0.746	0.798
AO	JFM	Hormozgan	0.868	0.868	1.351	0.888
AMO	JFM	Zabul	-0.789	0.789	2.166	0.629
SCAND	JFM	Hormozgan	0.755	0.755	0.967	0.888
QBO30Z	JFM	Shiraz	0.611	0.611	1.549	0.826
PDO	OND	Esfahan	-0.559	0.559	1.626	0.746
TSA	JFM	Kerman	0.532	0.532	0.747	0.746
AMM	JFM	Minab	0.478	0.478	0.971	0.765
EP-NP	JFM	Hormozgan	-0.449	0.449	1.228	0.888
PNA	JFM	Jask	-0.434	0.434	1.430	0.543
TNA	JFM	Hormozgan	0.430	0.430	1.138	0.888
EAWR	OND	Ghuchan	0.384	0.384	1.227	0.628
SCAND	AMJ	Sanandaj	0.583	2.190	1.533	0.633
EP-NP	AMJ	Shiraz	0.342	2.000	0.451	0.451
MEI	AMJ	Ghuchan	0.148	1.735	0.384	0.384
ONI	AMJ	Ghuchan	0.583	2.163	1.720	0.384
TNA	AMJ	Jask	0.342	1.133	1.719	0.225
AMM	AMJ	Jask	0.148	1.074	1.650	0.225
AMO	AMJ	Hormozgan	0.146	0.666	1.649	0.341
SCAND	AMJ	Saqqez	0.148	0.569	1.486	0.576
QBO30Z	AMJ	Shiraz	0.142	0.455	1.413	0.451
PDO	AMJ	Abadan	0.298	0.426	1.324	0.533
SOI	AMJ	Jask	-0.096	0.229	1.288	0.225
TSA	AMJ	Kish	0.253	0.356	1.195	0.235
EAWR	AMJ	Tabriz	0.250	0.366	0.951	0.533
PNA	AMJ	Shiraz	0.111	0.223	0.901	0.451
AMO	JFM	Zabol	0.133	0.203	2.166	0.629
QBO30Z	JFM	Shiraz	-0.225	0.126	1.549	0.826
PNA	JFM	Jask	-0.169	0.256	1.430	0.543
AO	JFM	Hormozgan	-0.789	0.563	1.351	0.888
EP-NP	JFM	Hormozgan	0.611	0.563	1.228	0.888
TNA	JFM	Hormozgan	-0.434	0.325	1.138	0.888
AMM	JFM	Minab	0.868	0.752	0.971	0.765
SCAND	JFM	Hormozgan	-0.449	0.415	0.967	0.888
EAWR	JFM	Shiraz	0.430	0.585	0.838	0.826
TSA	JFM	Kerman	0.478	0.611	0.747	0.746
ONI	JFM	Kish	0.755	0.869	0.746	0.798
SOI	JFM	Kerman	0.284	0.426	0.744	0.746
PDO	JFM	Shiraz	0.532	0.601	0.671	0.826
MEI	JFM	Kerman	-1.074	0.856	0.664	0.746
QBO30Z	OND	Saravan	-1.163	0.926	2.700	0.158
PDO	OND	Esfahan	0.519	0.430	1.626	0.746
SCAND	OND	Esfahan	-1.133	0.754	1.518	0.746
MEI	OND	Ghuchan	0.201	0.421	1.239	0.628
EAWR	OND	Maragheh	-0.559	0.745	1.227	0.628
EAWR	OND	Tabriz	0.456	0.556	1.114	0.786

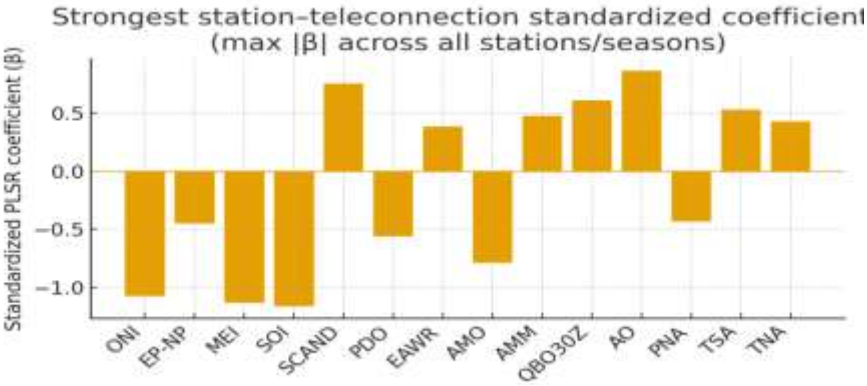

Figure 5. Standardized β at the strongest station for each teleconnection (sign denotes direction).

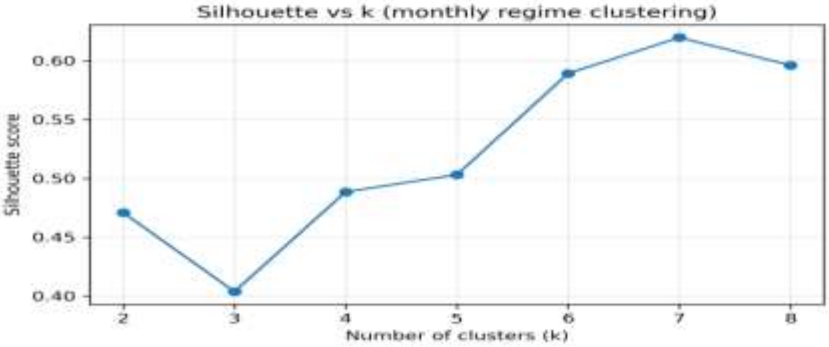

Figure 6. Silhouette score as a function of cluster number (k).

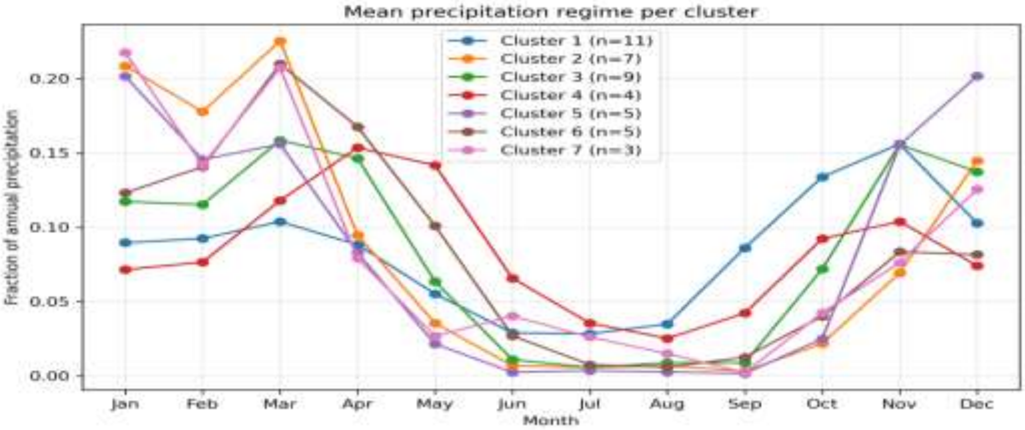

Figure 7. Cluster-mean fraction of annual precipitation by month.

Table 6 depicts quantitative descriptors of the seven precipitation-regime clusters.

4-3-1. Cluster-wise interpretation

Cluster 1 (n=11) comprises the Caspian littoral and the Alborz–Tehran corridor (Sari, Tehran, Imam-Airport, Rasht, Semnan, Gazvin, Karaj, Bandar-Torkaman, Ramsar, Anzali, and Abali). The regime is distinctly bimodal within the cold season, with a pronounced late-autumn/early-winter maximum in November (≈15.6% of annual totals) and a secondary spring shoulder around March (≈10.4%). Summer rainfall is negligible (JJA ≈8.7%), indicating dominance of westerly baroclinic systems and Caspian moisture recycling, modulated by Alborz orographic uplift.

Cluster 2 (n=7; Kerman, Birjand, Shiraz, Zabol, Hormozgan, Yazd, and Minab) represents the arid to semi-arid interior and southern fringe. It exhibits the sharpest concentration of precipitation in late winter–early spring, peaking in March (≈22.5%), while April–September collectively contribute <20% (JJA ≈1.7%). This canonical Mediterranean-driven regime is consistent with strong subtropical subsidence and minimal warm-season convection.

Cluster 3 (n=9; central plateau and western Zagros transition: Qom, Saveh, Kermansah, Hamedan, Gasreshirin, Esfahan, Dehloran, Arak, and Ilam) shows a broader wet season. March–April dominates (peak in March ≈15.8%; MAM ≈36.9%), yet autumn and early winter remain non-trivial (SON ≈20.9%; DJF ≈31.5%). Compared with Cluster 2, the wet peak is less acute and inter-monthly variability within the cluster is lower, implying a mixed control of Mediterranean troughs and local orographic/convective enhancement.

Cluster 4 (n=4; north-western highlands: Khoy, Tabriz, Uromyieh, and Jolfa) features a delayed spring maximum (April ≈15.4%; May ≈14.2%) along with modest October–November contributions. The relatively elevated MAM fraction (≈45.6%) reflects persistent frontal activity and snow–rain transitions over elevated terrain; JJA remains minor (≈3.4%).

Cluster 5 (n=5; Persian Gulf coast and adjacent uplands: Yasuj, Abadan, Sahrekord, Kish, and Busehr) is strongly winter-bound, with December–February accounting for ≈49.9% and a dual maximum in December–January (≈20% each). The nearly rain-free summer (JJA ≈0.7%) underscores the role of Gulf-sourced moisture advected by mid-latitude cyclones and amplified by Zagros uplift.

Cluster 6 (n=5; north-eastsector: Nyshabur, Miamy, Mashad, Ghuchan, and Golestan) presents a clear spring-centric regime. March and April together contribute ≈38.1%, and the MAM share reaches ≈48.3%, whereas JJA is minimal (≈4.5%). This timing is coherent with the seasonal southward extension of westerly storm tracks into north-eastern Iran and orographic triggering.

Cluster 7 (n=3; south-eastern monsoon-fringe stations: Jask, Saravan, and Zahedan) is the only regime displaying a discernible warm-season tail (June ≈4.0%; JJA ≈3.1%) in addition to a winter–spring peak (January–March ≈55.3%). The expanded wet window is compatible with episodic Arabian Sea tropical intrusions and pre-monsoon convection superimposed on the dominant westerly signal (Mehrvarz et al., 2025; Tao et al., 2025; Spuler et al., 2024).

At the final stage, composite anomaly maps of various atmospheric levels that play a significant role in precipitation, particularly those identified as most influential through the PLSR method, will be thoroughly discussed and interpreted. These maps have been generated using advanced Python-based software, covering the spatial domain extending from the eastern Atlantic to eastern Afghanistan, with all map legends and annotations clearly defined. The analysis encompasses the impacts of teleconnection indices both on a monthly scale and as seasonal averages, while the meteorological stations included in the study area are denoted by black dots. Extreme positive and negative phases of teleconnection patterns are indicated by the thresholds $p > 75$ and $p < 25$, respectively. Owing to the extensive scope of the study and certain practical constraints, a selection of these maps has been subjected to detailed analysis and interpretation.

Table 6. Quantitative descriptors of the seven precipitation-regime clusters.

Cluster	n_stations	Peak month	Peak fraction	DJF fraction	MAM fraction	JJA fraction	SON fraction	Within-cluster L2 (mean)
1	11	Nov	0.156	0.285	0.247	0.092	0.376	0.027
2	7	Mar	0.225	0.531	0.356	0.019	0.094	0.065
3	9	Mar	0.159	0.37	0.368	0.025	0.236	0.026
4	4	Apr	0.154	0.222	0.413	0.126	0.238	0.017
5	5	Dec	0.202	0.549	0.26	0.009	0.182	0.053
6	5	Mar	0.21	0.345	0.478	0.04	0.136	0.017
7	3	Jan	0.217	0.485	0.313	0.081	0.121	0.053

4-3. Map Legend and Data Notes

All maps (in Figure 8) were rendered in Python across a domain spanning roughly 60°W–80°E and 10°–55°N. Legends identify magnitudes with continuous color bars: winds at 250 hPa are shown with arrow vectors, a reference scale (20 m s^{-1}) and a starred jet-core marker; 500-hPa geopotential height anomalies (dam) use warm colors for positive (H) and cool colors for negative (L); relative humidity anomalies (%) use a diverging palette (negative=drier, positive=moister); precipitation anomalies are in mm $month^{-1}$ (negative=decrease, positive=increase). Composite years are listed on each panel; HIGH corresponds to years with the index at or above the 75th percentile; LOW to at or below the 25th percentile. Because full gridded fields are not provided, we infer numerical ranges conservatively from the panel color bars and station-dense areas. Values below are visual estimates (order-of-magnitude, ±5–10 units) designed to capture the sign and typical amplitude of the composites; they do not represent formal pixel-wise statistics. Correlation signs are stated with respect to precipitation anomalies in the named region (Table 7). It is noteworthy that the relative humidity anomaly represents the mean anomaly of relative humidity across the 850, 700, and 500 hPa levels.

4-3-1. Interpretation of Teleconnection–Precipitation Cohesion

Either the AMM high-phase composite (OND) exhibits an equatorward-shifted, zonally elongated polar-front jet across North Africa into the Levant, or its low-phase counterpart relaxes the jet over Iran. Notwithstanding, the HIGH phase co-occurs with widespread negative precipitation anomalies across Iran, whereas the LOW phase shows the converse—neither the north nor the south bucking this basic sign pattern. On the other hand, the AMO low-phase composites in boreal winter (JFM) align with moister lower–mid-troposphere and positive rainfall departures across western, southern, and northern Iran, consistent with deeper troughing over the Black Sea–Caucasus corridor and enhanced baroclinicity (Figure 8 a, b, c, d, h).

Table 7. The Analysis of Teleconnections and their impacts in different levels of atmosphere.

Region	AMM (OND) HIGH	AMM (OND) LOW	AMO (JFM) LOW	AMO (JFM) HIGH	AMO (AMJ) HEIGHT
Western Iran	PR ↓ ~5–20 mm/mo; RH ↓ ~2–8%; co-located with strong 250-hPa jet → subsidence on right-entrance region (negative correlation)	PR ↑ ~10–30 mm/mo; RH ↑ ~3–10% (positive correlation)	PR ↑ ~10–25 mm/mo; RH ↑ ~5–12%; 500-hPa troughing to NW (positive correlation)	PR ↓ ~5–15 mm/mo; RH ↓ ~3–8% (negative correlation)	+Z500 in AMJ implies mid-tropospheric stability ↑ (dry tendency)
Eastern Iran	PR ↓ ~5–15 mm/mo; RH ↓ ~2–6% (negative)	PR ↑ ~5–20 mm/mo; RH ↑ ~3–8% (positive)	PR ↑ ~5–15 mm/mo; RH ↑ ~4–10% (positive)	PR ↓ ~5–10 mm/mo; RH ↓ ~2–6% (negative)	Mixed: weak anomalies; modest +Z500 → slight drying
Northern Iran	PR ↓ ~10–25 mm/mo along Alborz/Caspian rim (negative)	PR ↑ ~10–30 mm/mo Caspian fringe (positive)	PR ↑ ~5–20 mm/mo; RH ↑ ~3–8% (positive)	PR ↓ ~5–15 mm/mo; RH ↓ ~2–6% (negative)	AMJ: +Z500 over Europe; weak signals over N Iran
Southern Iran	PR ↓ ~5–15 mm/mo; RH ↓ ~2–6% (negative)	PR ↑ ~10–25 mm/mo; RH ↑ ~3–8% (positive)	PR ↑ ~10–20 mm/mo; RH ↑ ~4–10% (positive)	PR ↓ ~5–15 mm/mo; RH ↓ ~3–8% (negative)	+Z500 in AMJ → reduced ascent and moisture flux (dry tendency)

In AMJ, positive AMO-related height anomalies at 500 hPa imply increased static stability and suppressed ascent over much of Southwest Asia; the seasonal timing dovetails with Iran’s climatological dry season outside the Caspian rim, so only muted precipitation responses are expected. Conversely, in JFM during −AMO, the RH composites show basin-wide moistening (≈+5–15%), and the precipitation maps reveal scattered +10–30 mm $month^{-1}$ anomalies—particularly over western and southern provinces—implying constructive interference between synoptic forcing and moisture availability. The 250-hPa jets during AMM(HIGH) organize a right-entrance/left-exit dipole that, over Iran, often corresponds to subsidence and reduced column moisture, whereas during AMM (LOW) the weakened or poleward-retracted jet diminishes this suppression, enabling Mediterranean–Red Sea moisture fluxes to penetrate. For −AMO winters, negative North Atlantic SST anomalies reshape the Rossby wave source and downstream phase of the Eurasian wave train, deepening the mid-tropospheric trough over the Black Sea–Caucasus and favoring cyclogenesis and moisture convergence over Iran. Such dynamics are congruent with independent studies on Middle Eastern teleconnections and jet-precipitation coupling. Figures are represented in (Figure 8-a to j) from a1-a10. (Rousta et al., 2023; Asakereh & Ashrafi, 2023; Haleme et al., 2025).

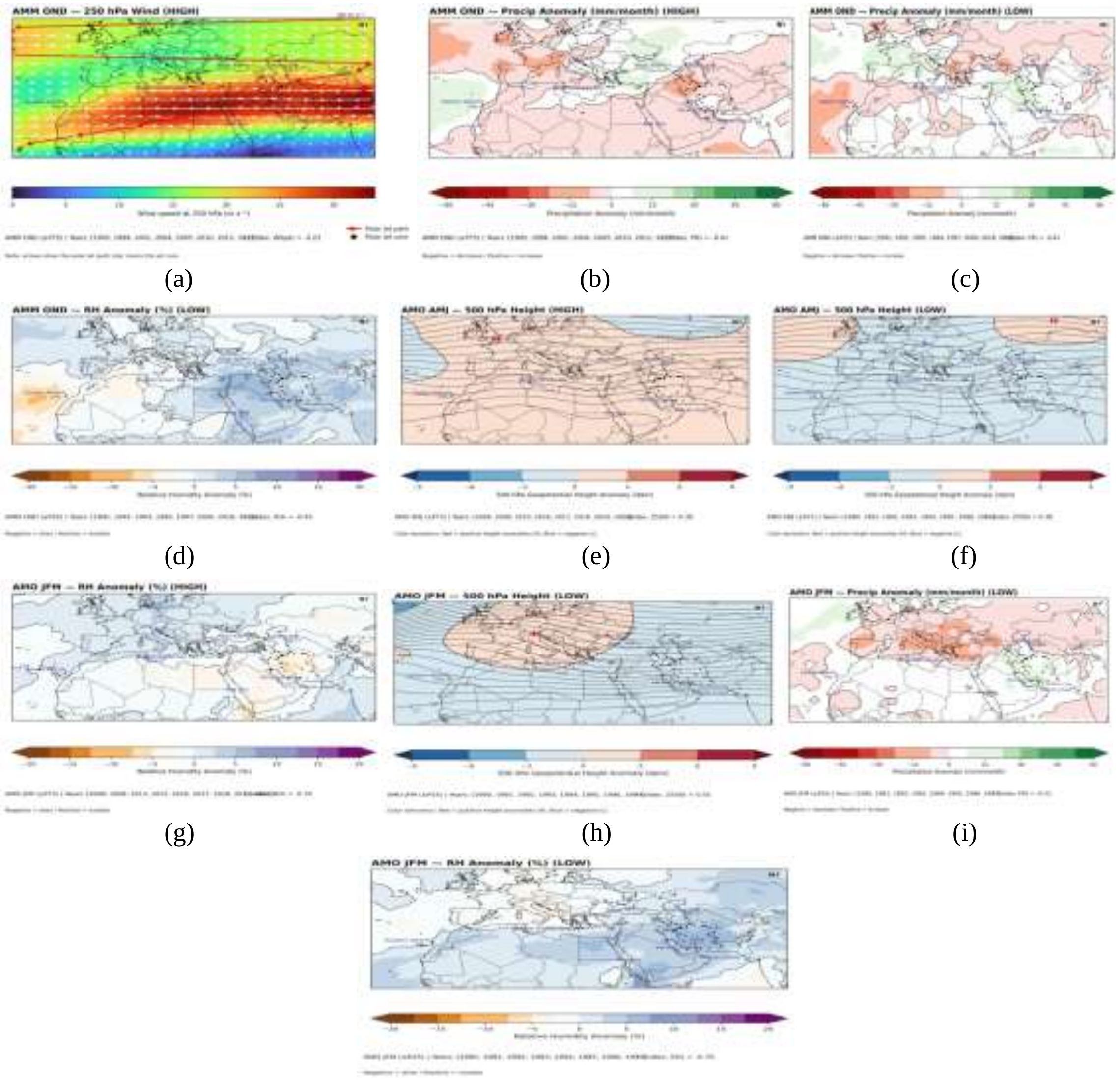

(a) (b) (c)

(d) (e) (f)

(g) (h) (i)

(j)

Figure 8. The analysis of different levels atmosphere. a) AMM (OND)-250 hpa wind (High), b) AMM (OND) -Precip Anomaly (High), c) AMM (OND) -Precip Anomaly (Low), d) AMM (OND)- RH Anomaly (Low), e) AMO (AMJ) - 500 hpa (High), f) AMO (AMJ)-500 hpa (Low), g) AMO (JFM)- RH Anomaly (High), h) AMO (JFM)-500 hpa (Low), i) AMO (JFM) -Precip- Anomaly (Low), j) AMO (JFM) RH -Anomaly (Low).

4-3-2. Interpretation of Teleconnection–Precipitation Cohesion (Part 2)

In Figure 9 provides an integrated composite anomaly assessment of the Atlantic Multidecadal Oscillation (AMO), East Atlantic/West Russia (EAWR), and East Pacific–North Pacific (EP/NP) indices in relation to Iranian precipitation variability (Chen & Song, 2018). The atmospheric parameters examined include 250 hPa wind fields, 500 hPa geopotential heights, and relative humidity anomalies averaged across 850, 700, and 500 hPa levels. Data visualizations were generated in Python for a domain spanning from the eastern Atlantic to eastern Afghanistan. Stations appear as black dots, while composite phases are designated by p≥75 (HIGH) and p≤25 (LOW). The results demonstrate that upper-level circulation and moisture anomalies coherently modulate rainfall patterns across Iran, particularly within the western and southern provinces. Color semantics are standardized across all composites: warm tones denote positive anomalies (e.g., ridging or dryness), while cool tones denote negative anomalies (e.g., troughing or moistening). The 250 hPa wind maps display arrow vectors indicating direction, a 20 m s^{-1} reference vector, and a black star representing the jet core. Precipitation anomalies are expressed in mm month^{-1} (positive = increase), and relative humidity anomalies in percentage, computed as the mean across the 850, 700, and 500 hPa levels. Geopotential height (Z500) values are in decameters (dam).

Either the AMO or the EAWR index strongly modulates precipitation anomalies across Iran through shifts in upper-level dynamics. During AMO-LOW winters, a cyclonic anomaly over the Caucasus–Caspian sector enhances vertical motion, leading to +15–40 mm month^{-1} rainfall increases and +5–15 % RH anomalies in western and southern Iran. Conversely, AMO-HIGH phases suppress rainfall (−10 to −25 mm month^{-1}) with anticyclonic ridging and weakened westerly flow. Notwithstanding, northern Iran occasionally exhibits localized moistening under residual Black Sea influence.

On the other hand, the EAWR pattern exerts pronounced control over jet positioning. At 250 hPa, the HIGH phase jet intensifies and shifts northward (core velocities > 35 m s^{-1}), diverting storm tracks poleward and inducing regional dryness. The LOW phase, featuring a weaker and equatorward jet, facilitates Mediterranean moisture advection and enhanced precipitation over the Zagros region (+15–35 mm month^{-1}). Geopotential fields during EAWR-LOW display distinct troughing, while positive Z500 anomalies (EAWR-HIGH) confirm a blocking regime suppressing ascent.

In contrast, the EP/NP index primarily influences springtime (AMJ) circulation through a widespread negative Z500 anomaly extending from North Africa into Iran, implying stronger troughing and vertical instability. However, because this coincides with the climatologically dry season, rainfall response is relatively modest (±10–15 mm month^{-1}). Either through amplification or jet weakening under EP/NP-HIGH alters convective thresholds, yet the broader moisture supply remains limited (Figure 9- a to j) (Lu et al., 2020; Zittis, 2018).

4-3-2-1. Regional Summary (Part2)

- Western Iran (Kermanshah, Ilam, Khuzestan): Wet under AMO-LOW and EAWR-LOW (+20–40 mm month^{-1}), dry under EAWR-HIGH.
- Eastern Iran (Khorasan and Sistan–Baluchestan): Limited sensitivity; slight dryness under AMO-HIGH.
- Northern Iran (Caspian provinces): Mild positive departures under EAWR-LOW and AMO-LOW.
- Southern Iran (Fars, Hormozgan): Enhanced rainfall (+10.25 mm month^{-1}) in EAWR-LOW and AMO-LOW years.

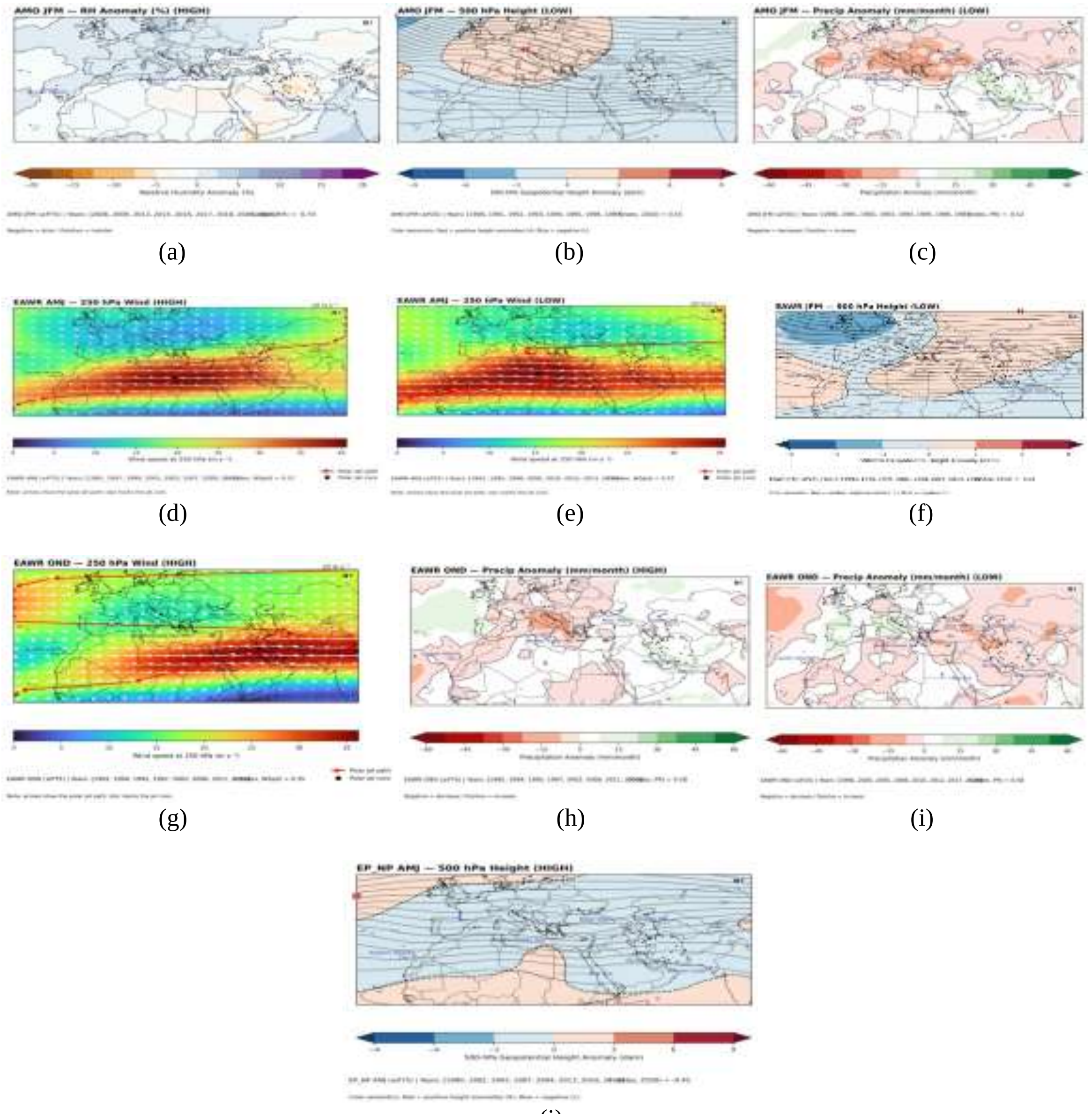

(a) (b) (c)

(d) (e) (f)

(g) (h) (i)

(j)

Figure 9. The analysis of different levels atmosphere (Part2). a) AMO (JFM)- RH- Anomaly (High), b) AMO (JFM)- 500 hpa (Low), c) AMO (JFM)- Precip Anomaly (Low), d) EAWR (AMJ)-250 hpa Wind (High), e) EAWR (AMJ) 250 hpa Wind (Low), f) EAWR (JFM) -500 hpa (Low), g) EAWR (OND) 250 hpa (High) h) EAWR (OND) Precip Anomaly (High), i) EAWR (OND) Precip Anomaly (Low), j) EP-NP (AMJ) 500 hpa (High).

4-3-3. Interpretation of Teleconnection–Precipitation Cohesion (Part 3)

Figure 10 provides a composite anomaly-based analysis of three major global teleconnections—East Pacific–North Pacific (EP/NP), Multivariate ENSO Index (MEI), and Oceanic Niño Index (ONI)—to elucidate their atmospheric influence on precipitation variability over Iran. The research integrates multiple atmospheric parameters including 500 hPa geopotential height, 250 hPa wind flow, and relative humidity averaged across 850, 700, and 500 hPa levels. Maps were generated using advanced Python visualization techniques for the region extending from the eastern Atlantic to eastern Afghanistan. Precipitation and moisture anomalies were evaluated for HIGH ($p \geq 75$) and LOW ($p \leq 25$) teleconnection phases to diagnose the spatial coherence of large-scale circulation anomalies. The composite analysis reveals that the EP/NP, MEI, and ONI indices substantially influence upper- and mid-tropospheric circulation patterns over Iran, particularly during winter (JFM) and autumn (OND) seasons. Under EP/NP-HIGH conditions ($p \geq 75$), precipitation anomalies demonstrate localized wet signals (+15–30 mm month^{-1}) over southern Iran, accompanied by slight moisture enhancement (+5–10 % RH), implying strengthened westerly advection of maritime air from the eastern Mediterranean.

The MEI composites exhibit a markedly coherent tropospheric response. During OND-HIGH phases, a negative geopotential height anomaly (ridge) prevails over North Africa and the western Mediterranean, inducing subsidence and positive precipitation anomalies (+15 to +40 mm month^{-1}) across western and central Iran. Conversely, the LOW phase decreases trough activity, yielding lower precipitation rates (-20–45 mm month^{-1}) and a 5–15 % decrease in relative humidity throughout the southern basins and the Zagros range. These anomalies indicate that El Niño-like conditions (positive MEI) inclines rainfall, whereas La Niña-like episodes declines wetter winters.

The ONI patterns further corroborate this inverse linkage. ONI-HIGH composites during OND display a mid-tropospheric ridge extending from the eastern Atlantic into the Levant, increasing precipitation over Iran's interior and northern highlands. During ONI-LOW (La Niña) events, adecrease trough over the eastern Mediterranean supports moist air transport toward Iran, producing rainfall deficiency of up to -50 mm month^{-1} in the west and southwest. Relative humidity anomalies at AMJ HIGH phase remain modest (-5–10 %), suggesting that the post-ENSO recovery period primarily affects convection rather than large-scale moisture content.

4-3-3-1. Regional Synthesis

The tri-index composite suggests that tropical Pacific oscillations (MEI, ONI) modulate the synoptic circulation reaching Iran through planetary-scale Rossby wave propagation. The downstream extension of the subtropical jet under El Niño conditions fosters cyclonic dominance, whereas La Niña episodes shift the anticyclonic southward, weakening Mediterranean cyclogenesis. The EP/NP pattern, although subtler, reinforces these Pacific teleconnections by modulating the North Pacific ridge and the entrance region of the westerlies feeding into the Middle East. Either combination of MEI-LOW and EP/NP-LOW or concurrent ONI-LOW yields the driest Iranian winters, aligning with decreased upward motion and positive 500 hPa height anomalies (Figure 10 a to j).

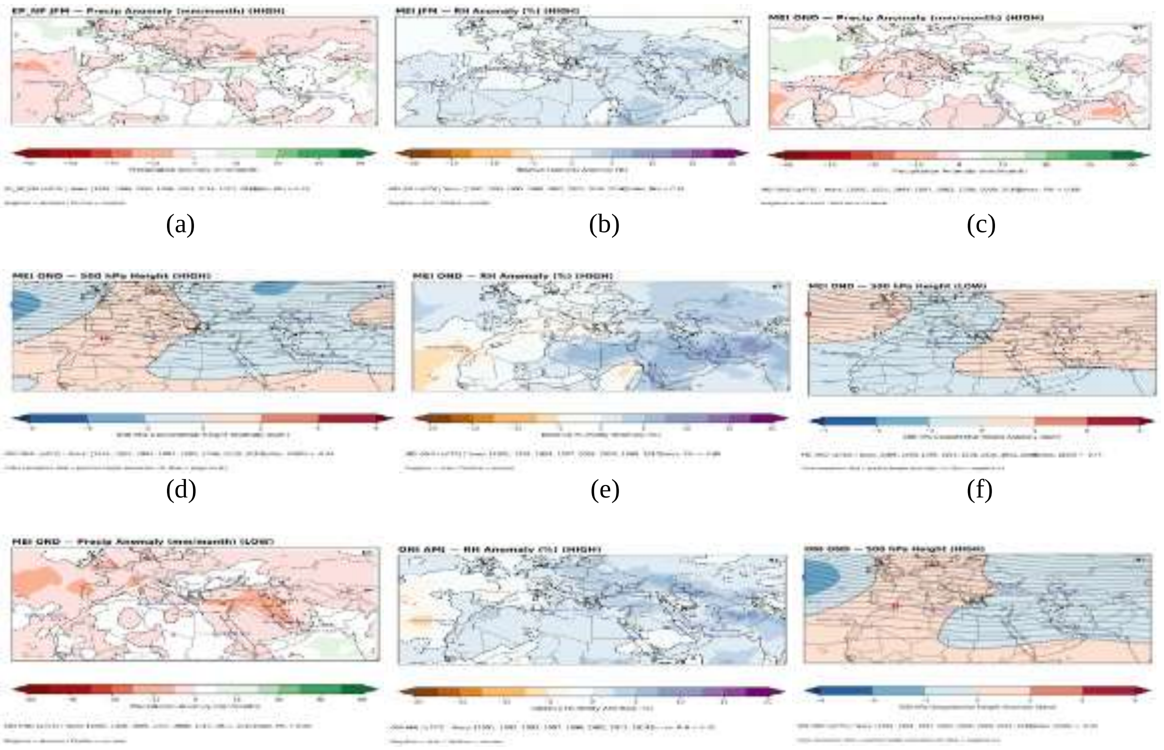

(a) (b) (c)

(d) (e) (f)

(g) (h) (i)

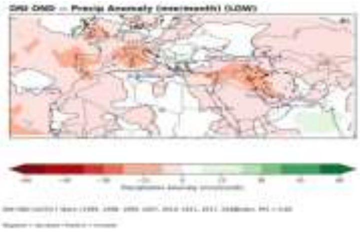

(j)

Figure 10. The analysis of different levels atmosphere (Part 3). a) EP-NP (JFM) Precip Anomaly (High), b) MEI (JFM) RH-Anomaly (High), c) MEI (OND) Precip -Anomaly (High), d) MEI (OND) 500 hpa (High), e) MEI (OND) -RH -Anomaly (High), f) MEI (OND) 500 hpa (Low), g) MEI (OND) Precip-Anomaly (Low), h) ONI (AMJ) RH-Anomaly (High), i) ONI (OND) 500hpa (High), j) ONI (OND)-Precip Anomaly (Low).

4-3-4. Integrated interpretation of the composites

In Figure (11- a to j) depicts percentile-based composites of circulation and hydroclimatic anomalies associated with the Scandinavian pattern (SCAND) and the Southern Oscillation Index (SOI) over the Mediterranean–Red Sea–Iran domain. The maps focus on years when each index exceeds its upper quartile (≥P75; “HIGH” phase) or falls below its lower quartile (≤P25; “LOW” phase), thus isolating the tails of the distribution where teleconnections are expected to be strongest. Stippled or dashed areas denote regions where the anomalies pass standard significance thresholds (typically ≥90% confidence), while the black dots indicate the locations of the rain-gauge stations used in the regional analysis. All anomalies are expressed relative to a common climatology: precipitation in mm month^{-1}, relative humidity (RH) in percentage points, 500-hPa geopotential height in decameters (dam), and 250-hPa wind speed in m s^{-1}.

At the panel bottoms, the linear correlation between the index and the field averaged over the observational network is given as r (index, variable). These values allow a quantitative assessment of the strength of the teleconnections. Squared correlations (r^2) provide the fraction of variance in the regional mean field that can be linearly explained by each index:

- SCAND–AMJ precipitation (HIGH): $r = 0.50 \Rightarrow r^2 \approx 0.25$, i.e. ≈25 % of the interannual variance in spring–early-summer precipitation over the station network is linearly associated with SCAND.
- SCAND–JFM 250-hPa wind speed (HIGH): $r = -0.28 \Rightarrow r^2 \approx 0.08$.
- SOI–AMJ 500-hPa height (LOW): $r = 0.32 \Rightarrow r^2 \approx 0.10$.
- SOI–JFM precipitation (HIGH): $r = -0.31 \Rightarrow r^2 \approx 0.10$.
- SOI–JFM RH (HIGH): $r = -0.38 \Rightarrow r^2 \approx 0.14$.
- SOI–JFM precipitation (LOW): $r = -0.31 \Rightarrow r^2 \approx 0.10$.
- SOI–OND 500-hPa height (HIGH): $r = 0.44 \Rightarrow r^2 \approx 0.19$.
- SOI–OND precipitation (HIGH) and RH (HIGH): $r = -0.60 \Rightarrow r^2 \approx 0.36$.
- SOI–OND precipitation (LOW): $r = -0.60 \Rightarrow r^2 \approx 0.36$.

Thus, the autumn SOI signal exerts the most statistically coherent control on the hydroclimate of the station network, explaining roughly one-third of the interannual variance in both precipitation and near-surface humidity. In contrast, the winter SCAND–jet relationship and the late-spring SOI–mid-tropospheric height link are weaker but still non-negligible, accounting for roughly 8–10 % of the variance.

4-3-4-1. SCAND–AMJ precipitation anomaly (HIGH) (a)

The AMJ composite for high SCAND phases (Figure 11-a) reveals predominantly negative precipitation anomalies across the Mediterranean basin, the Red Sea and most of Southwest Asia, with deficits typically in the range of −10 to −30 mm month^{-1} and locally below −45 mm month^{-1} in parts of north-eastern Europe and western Russia. Over the Iranian station network (black dots), the pattern is remarkably coherent: nearly the entire region lies within a dry anomaly envelope, indicating a systematic suppression of late-spring to early-summer rainfall.

Localized positive precipitation anomalies appear over parts of the western Iberian Peninsula and adjacent eastern Atlantic, but these are spatially confined and generally of smaller magnitude than the widespread drying over the eastern Mediterranean and the Iranian Plateau. This dipolar structure is consistent with the meridional wave train associated with the positive SCAND phase, which favors anticyclonic ridging over eastern Europe–western Asia and enhanced storminess over the North Atlantic and western Europe.

The relatively high correlation (r = 0.50) between the SCAND index and regional mean AMJ precipitation implies that years with a strong positive SCAND are typically 25 % drier or wetter than average purely due to SCAND-related variability, when measured in terms of variance. From a practical standpoint, this underscores the potential predictability of spring rainfall over Iran and the eastern Mediterranean from forecasts of the SCAND pattern.

4-3-4-2. SCAND–JFM 250-hPa wind (HIGH) (b)

The winter composite of 250-hPa wind speed for high SCAND phases (Figure 11-b) shows an intensified subtropical jet extending from North Africa across the Red Sea and the northern Arabian Peninsula towards Iran, with wind speeds exceeding 35–40 m s^{-1} along the jet core. The polar jet path, highlighted by arrows and a star marking its maximum, is displaced equatorward relative to its climatological position, sweeping across the Mediterranean, the northern Red Sea and into Southwest Asia.

This configuration yields two important dynamical consequences: (i) enhanced upper-level westerlies over North Africa and the Middle East, favoring strong vertical wind shear and baroclinicity along the jet axis; and (ii) suppressed synoptic wave breaking over the eastern Mediterranean, as the jet becomes more zonal and the entrance/exit regions of the jet shift away from key storm-genesis areas.

The modest but significant negative correlation (r = −0.28) between SCAND and regional mean 250-hPa wind speed suggests that, over the domain used in the correlation calculation, positive SCAND tends to be associated with slightly weaker upper-tropospheric winds when averaged broadly, even though the composite map exhibits strong localized maxima along the jet core. This apparent contradiction reflects the spatial heterogeneity of the response: acceleration along the jet axis coexists with wind reductions poleward of the jet, so the domain-mean response is muted.

4-3-4-3. SOI–AMJ: 500-hPa geopotential height (LOW) (c)

During low SOI phases in AMJ (Figure 11-c; El Niño-like conditions), the 500-hPa low anomaly composite is characterized by negative geopotential height anomalies across much of the eastern Mediterranean, the Middle East and Iran, with amplitudes of about -3 to -6 dam. A weaker negative anomaly appears over parts of the eastern Atlantic, implying an enhanced zonal gradient in mid-tropospheric heights.

This pattern is indicative of anomalous cyclonic ridging over western Asia, which promotes upward motion and thereby persuades convective precipitation. The closed or nearly closed negative height contours extend across the Iranian station network, suggesting that the majority of stations experience a dynamically consistent subsidence regime in low-SOI springs. The correlation (r = 0.32; $r^2 \approx 10$ %) indicates that the SOI explains around 10 % of the interannual variance in regional springtime mid-tropospheric height, providing a physical bridge between tropical Pacific variability and the hydroclimate of Southwest Asia.

4-3-4-4. SOI–OND: 500-hPa geopotential height (HIGH) (g)

In high SOI autumns (OND; La Niña-like conditions, Figure 11-g) the 500-hPa height composite exhibits a broad, statistically significant positive height anomaly over the Mediterranean, Red Sea and Iran, with maxima around +6 to +9 dam. A compensating negative anomaly is evident over the North Atlantic, forming a zonally elongated dipole. This structure resembles the canonical response of the Euro-Mediterranean circulation to La Niña, wherein decreasing of the subtropical ridge over the Middle East is accompanied by a lack of the deepening of the North Atlantic trough.

The correlation between OND SOI and regional 500-hPa height is relatively strong (r = 0.44; $r^2 \approx 19$ %), implying that nearly one-fifth of the observed interannual variability in autumn mid-tropospheric heights over the station network is linearly linked to the tropical Pacific.

4-3-4-5. SOI–JFM precipitation and RH (HIGH) (d, e)

For high SOI winters (JFM; La Niña-like conditions, Figure 11-g, d) the composites reveal a coherent drying and desiccation signal. The JFM precipitation anomaly map for high SOI shows negative anomalies of about −15 to −45 mm $month^{-1}$ across most of the Mediterranean basin, the Red Sea and Southwest Asia, including virtually all black-dot stations in Iran. Positive anomalies are restricted to small patches, such as parts of the Iberian Peninsula and the adjacent eastern Atlantic. The correlation ($r = -0.31$; $r^2 \approx 10$ %) indicates that high SOI winters are reliably associated with reduced rainfall over the Iranian network.

The corresponding RH composite displays negative anomalies of about −5 to −15 % along the eastern Mediterranean, the Red Sea and the Arabian Peninsula, with particularly pronounced deficits over the Eastern Mediterranean–Levant–northern Red Sea corridor. Over the station network the anomalies are mostly negative, signaling a widespread reduction in near-surface moisture availability. The correlation is stronger than for precipitation ($r = -0.38$; $r^2 \approx$ 14 %), implying that SOI explains roughly one-seventh of the variance in winter RH at the regional scale.

4-3-4-6. SOI–JFM precipitation (LOW) (f)

During low SOI winters (El Niño-like conditions, Figure 11-f) the JFM precipitation composite presents a broadly opposite pattern over the Mediterranean and North Atlantic, but the response over Iran and adjacent regions is more nuanced. Negative anomalies persist over the western Mediterranean and parts of Europe, whereas weakly positive precipitation anomalies emerge over parts of the Iranian Plateau and the northern Zagros, albeit with smaller magnitude than the deficits during high SOI. The correlation with regional mean precipitation remains negative ($r = -0.31$), suggesting that, for the specific averaging domain chosen, El Niño winters do not simply reverse the sign of the SOI–precipitation relationship; instead, they redistribute the anomalies, with compensating wet and dry regions that reduce the domain-mean signal.

4-3-4-7. SOI–OND precipitation and RH (HIGH) (g, h)

The OND high-SOI composites (Figures 11-g, h) exhibit the clearest and most statistically robust hydroclimatic signal. The OND precipitation map shows pervasive negative anomalies from the central Mediterranean eastwards across Turkey, northern Iraq and Iran, with deficits commonly in the −15 to −45 mm $month^{-1}$ range and locally approaching −60 mm $month^{-1}$. The Iranian station network lies almost entirely within these strongly negative anomalies.

The OND RH map reveals collocated negative anomalies of −5 to −15 % over the eastern Mediterranean, the Red Sea basin and the Iranian Plateau, highlighting a coherent drying of the free troposphere and boundary layer. For both variables the correlation with SOI reaches $|r| = 0.60$ ($r^2 \approx 36$ %), meaning that about one-third of the interannual variability in autumn precipitation and humidity over the station network is linearly associated with the SOI.

4-3-4-8. SOI–OND precipitation (LOW) (i, j)

In low SOI OND composites (El Niño-like conditions, Figure 11-i, j), the precipitation anomalies over the Iranian stations and the eastern Mediterranean are generally opposite in sign but weaker in magnitude, with modest positive anomalies over parts of Iran and neighboring areas. The domain-mean correlation remains negative ($r = -0.60$), reflecting that, when averaged over the full analysis domain, La Niña winters are much more efficient at producing coherent drying than El Niño winters are at producing widespread moistening.

4-3-5. Role of the Mediterranean Sea, Red Sea and regional moisture pathways

Across the composites, three key maritime regions emerge as mediators of the teleconnections. First, the Mediterranean Sea, which repeatedly lies beneath the core of the precipitation and RH anomalies; anticyclonic height anomalies suppress cyclone formation and frontal activity over the basin, decreasing both rainfall and humidity. Second, the Red Sea and eastern Mediterranean moisture corridor, where changes in the position and strength of the subtropical jet divert moisture away from the eastern Mediterranean–Red Sea–Iran corridor. Third, the Persian Gulf and Makran Coast, where persistent negative precipitation and RH anomalies during high-SOI phases suggest a reduction in moisture flux from the Gulf into Iran’s interior.

4-3-6. Implications for the Iranian station network

The black dots representing Iranian stations are consistently embedded within the main anomaly centers. Under high SCAND in AMJ, stations experience suppressed precipitation of roughly −10 to −30 mm month^{-1}, associated with anticyclonic ridging extending from eastern Europe into western Iran. Under high SOI in JFM and OND, stations are subject to a combination of reduced precipitation (up to −60 mm month^{-1} in OND) and lower RH (−5 to −15 %), superimposed on positive 500-hPa height anomalies and a reconfiguration of the upper-level jet. These conditions are conducive to compound heat–drought episodes and highlight the vulnerability of the region to La Niña-related droughts.

Overall, first, positive SCAND phases in AMJ are associated with widespread drying across the eastern Mediterranean, Red Sea and Iran, with SCAND explaining about 25% of the variance in regional spring precipitation. Second, low-SOI springs and high-SOI autumns generate robust positive 500-hPa height anomalies over the Middle East, indicative of strengthened subtropical ridges; these anomalies explain roughly 10–20 % of the regional mid-tropospheric height variance. Third, high-SOI phases, particularly in OND, yield strongly negative precipitation and RH anomalies over the Mediterranean–Red Sea–Iran domain, with the SOI accounting for up to 36 % of the variance in these fields. Finally, the combination of statistically significant correlations, physically coherent anomaly patterns and consistency with recent literature suggests that both SCAND and SOI indices are valuable predictors for seasonal hydroclimate outlooks in the Mediterranean–Red Sea–Iran region (Alizadeh, & Mousavizadeh, 2025; Almaashi *et al*., 2024; Francis & Fonseca, 2024; Hoell et al., 2024; Lee et al., 2023; Magnini et al., 2024; Pang et al., 2023; Vicente-Serrano et al., 2025).

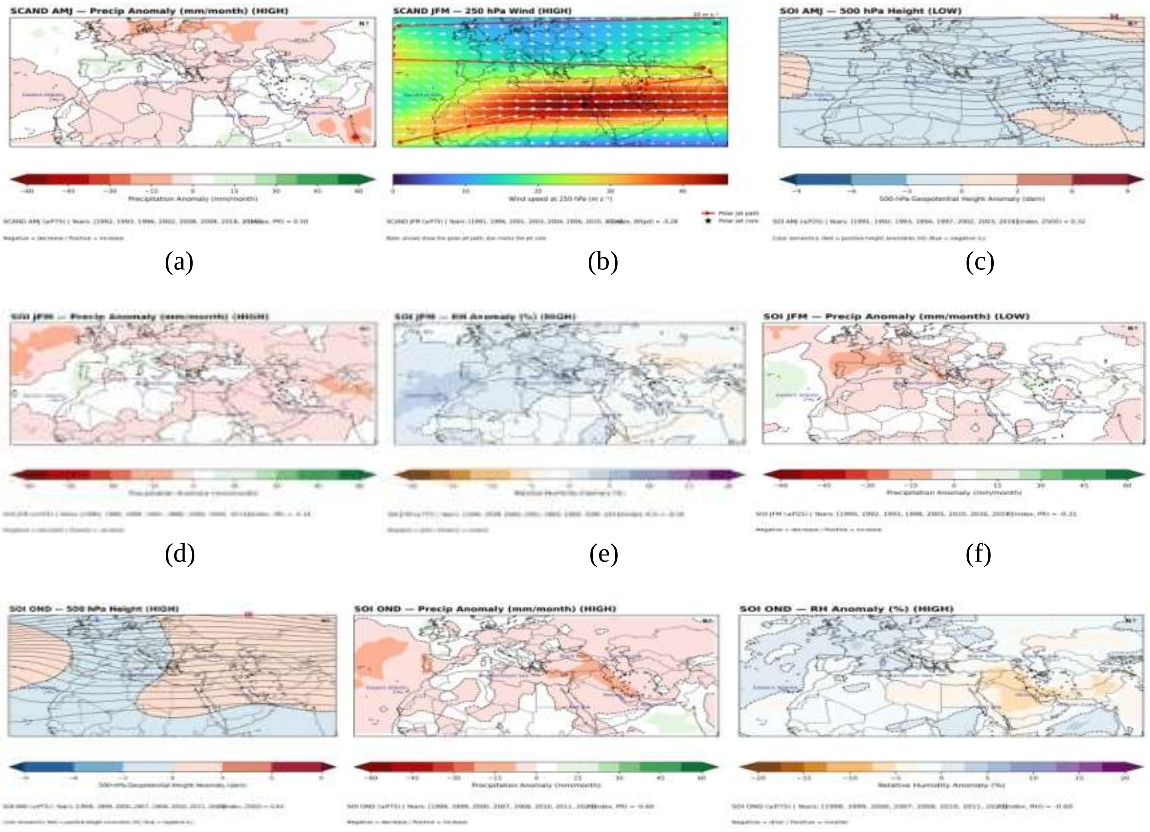

(a) (b) (c)

(d) (e) (f)

(g) (h) (i)

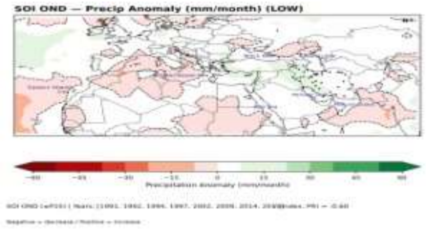

(j)

Figure 11. The analysis of different levels atmosphere (last part). a) SCAND (AMJ) -Precip Anomaly (High), b) SCAND (JFM) -250 hpa Wind (High), c) SOI (AMJ) 500 hpa (Low), d) SOI (JFM) -Precip Anomaly 9High), e) SOI (JFM) -RH Anomaly (High), f) SOI (JFM) -Precip Anomaly (Low), g) SOI (OND) -500 hpa (High), h) SOI (OND)-Precip Anomaly (High), i) SOI (OND) -RH Anomaly (High), j) SOI (OND) Precip-Anomaly (Low)

5. Conclusion

The station-resolved PLSR results show that Iranian rainfall is a teleconnection-imprinted field whose explainable variance is largest in the core wet season. Winter (JFM) achieves the highest mean skill (R^2=0.416; range 0.203–0.888), followed closely by autumn (OND, mean R^2=0.405), whereas spring (AMJ) remains weakly forced (mean R^2=0.287), attesting to the growing dominance of mesoscale and local processes after the winter storm-track decays. VIP and β diagnostics jointly identify ENSO-family indices, AMO, and EP-NP as the principal winter controls, SCAND as the defining spring modulator, and ENSO plus EAWR as the leading autumn drivers. The strongest station-level couplings—negative SOI/MEI over Kerman ($|\beta|\approx1.1$–1.2) and ONI over Kish ($\beta\approx-1.07$) in JFM, and negative PDO over Isfahan in OND—provide geographically explicit targets for seasonal outlooks, especially for drought-prone southern and southeastern basins. Regime clustering further partitions Iran into seven coherent rainfall calendars, clarifying where teleconnection impacts translate into distinct seasonal water budgets. Overall, methodological pluralism (CCA→PLSR→clustering, and PCA/SOM cross-checks for circulation patterns) is essential to preserve low-amplitude yet hydrologically potent signals, and it offers a defensible, physically grounded pathway toward station-scale forecasting and risk management.

References

Alizadeh, O., & Mousavizadeh, M. (2025). Impact of ENSO on extreme precipitation in Southwest Asia. *Global and Planetary Change,* 244, 104645. https://doi.org/10.1016/j.gloplacha.2024.104645

Almaashi, A. K., Hasanean, H. M., & Labban, A. H. (2024). Long-Term Teleconnections Between Global Circulation Patterns and Interannual Variability of Surface Air Temperature over Kingdom of Saudi Arabia. *Atmosphere,* 15(11), 1310. https://doi.org/10.3390/atmos15111310

Anstey, J. A., Banyard, T. P., Butchart, N., ALLen, S. & Gray, L. J. (2021). Prospect of increased disruption to the QBO in a changing climate. *Geophysical Research Letters,* 48(13), e2021GL093058. https://doi.org/10.1029/2021GL093058

Araghi, A., Mousavi-Baygi, M., Adamowski, J., & Martinez, C. (2017). Association between three prominent climatic teleconnections and precipitation in Iran using wavelet coherence. *International Journal of Climatology,* 37(6), 2809–2830. https://doi.org/10.1002/joc.4881

Asakereh, H., & Ashrafi, S. (2023). An investigation into trends in frequency and proportion of different durations of various types of extreme precipitation in Iran. *Meteorological Applications,* 30(1), e2117. https://doi.org/10.1002/met.2117

Azizi, Gh., Cheharara, T., & Safarrad, T. (2014). Simultaneous effect of NAO and SOI phases on Iran's climate. *Geography and Environmental Sustainability,* 12(4), 43-56. https://doi.org/18(16), 3229-3239.

Agarwal, A., Caesar, L., Marwan, N., Maheswaran, R., Merz, B., & Kurths, J. (2019). Networkbased identification and characterization of teleconnections on different scales. *Scientific Reports,* 9, 8808. https://doi.org/10.1038/s41598-019-45423-5

Bahrami, F., Ranjbar Saadatabadi, A.,

Meshkatee, A. H., & Kamali, G. (2020). The impact of ENSO phase transition on the atmospheric circulation, precipitation and temperature in the Middle East autumn. *Asia-Pacific Journal of Atmospheric Sciences,* 56(3), 439-453. https://doi.org/10.1007/s13143-019-00149-2

Baldwin, M. P., Ayarzagüena, B., Birner, T., Butchart, N., Butler, A. H., Charlton-Perez, A., WIlcox I.J. & Wilcox, L. J. (2021). Sudden stratospheric warmings. *Reviews of Geophysics,* 59(1), e2020RG000708. https://doi.org/10.1029/2020RG000708

Bannayan, M., Sanjani, S., Alizadeh, A., Lotfabadi, S. S., &Mohamadian, A. (2010). Association between climate indices, aridity index, and rainfed crop yield in northeast of Iran. *Field crops research,* 118(2), 105-114. https://doi.org/10.1016/j.fcr.2010.04.011

Baxter, S., & Nigam, S. (2015). Key role of the North Pacific Oscillation/West Pacific pattern in generating the extreme 2013–2014 North American winter. *Journal of Climate,* 28(20), 8109–8117. https://doi.org/10.1175/JCLI-D-14-00726.1

Bueso, D., Piles, M., & Camps-Valls, G. (2020). Nonlinear PCA for spatio-temporal analysis of Earth observation data. *IEEE Transactions on Geoscience and Remote Sensing,* 58(8), 5752-5763. https://doi.org/10.1109/TGRS.2020.2969813

Cai, Q., Li, F., Li, J., Liu, Y., & Sun, C. (2022). Influence of the Quasi-Biennial Oscillation on the spatial structure of the Arctic Oscillation in boreal winter. *Journal of Geophysical Research: Atmospheres,* 127(15), e2021JD035564. https://doi.org/10.1029/2021JD035564

Camps-Valls, G., & Bruzzone, L. (Eds.). (2009). Kernel methods for remote sensing data analysis. John Wiley & Sons.

Chen, S., & Song, L. (2018). Impact of the winter North Pacific Oscillation on the surface air temperature over Eurasia and North America: Sensitivity to the index definition. *Advances in Atmospheric Sciences,* 35(6), 702–712. https://doi.org/10.1007/s00376-017-7111-5

Dalelane, C., Paxian, A., Senande, M., Sanfiz, S., Rodríguez Guisado, E., Wandel, J., & Tyagi, A. (2025). Targeted Teleconnections and their Application to the Postprocessing of Climate Predictions. *EGUsphere,* 2025, 1-23. https://doi.org/10.5194/egusphere-2025-3664

Dehghani, M., Salehi, S., Mosavi, A., Nabipour, N., Shamshirband, S., & Ghamisi, P. (2020). Spatial analysis of seasonal precipitation over Iran: Co-variation with climate indices. *ISPRS International Journal of Geo-Information,* 9(2), 73. https://doi.org/10.3390/ijgi9020073

Ebrahimi, A., Rahimi, D., & Gushchina, D. (2023). Analysis of atmosphere‑ocean interaction on cold season precipitation in Iran. *Environmental Earth Sciences,* 82(8), 192. https://doi.org/10.1007/s12665-023-10858-7

Francis, D., & Fonseca, R. (2024). Recent and projected changes in climate patterns in the Middle East and North Africa (MENA) region. *Scientific Reports,* 14(1), 10279. https://doi.org/10.1038/s41598-024-60976-w

Geng, T., Cai, W., Wu, L., Zheng, X.-T., Santoso, A., & Yang, K. (2022). Emergence of changing Central-Pacific and Eastern-Pacific ENSO under greenhouse warming. *Nature Communications,* 13, 5946. https://doi.org/10.1038/s41467-022-33930-5

Haleme, K. G., Al-Dulaimi, S. Z., Razzaq, A. S. A. A., &Algayssi, K. A. A. A. (2025). The Relationship Between Large-Scale Relative Vorticity Fields and Rainfall in Syria During the Period, 1980-2020. *The Arab World Geographer,* 28(1), 62-77.

Han, Y., Ma, Y., Wang, Z., Xie, Z., Sun, G., Wang, B., Liu, J. & Fan, Y. (2021). Variation characteristics of temperature and precipitation on the northern slopes of the Himalaya region from 1979 to 2018. *Atmospheric Research,* 253, 105481. https://doi.org/10.1016/j.atmosres.2021.105481

Heidari, S., Karimi, M., Azizi, G., &Shamsipour, A. A. (2024). Impact of Westerly Winds Troughs and Ridges on Droughts Extent in Iran. *Geography and Environmental Planning,* 35(3), 161-188.

https://doi.org/10.22108/gep.2024.142104.1655

Heydari, A., Nazemosadat, M. J., & Hosseinzadehtalaei, P. (2025). Climate Change in the Middle East and the West Indian Subcontinent: Geographic Interconnections and the Modulation Roles of the Extreme Phases of the Atlantic Meridional Oscillation (AMO) and the Monsoon Cloudiness. *Climate,* 13(11), 221. https://doi.org/10.3390/cli13110221

Hoell, A., Robinson, R., Agel, L., Barlow, M., Breeden, M., Eischeid, J., ... & Quan, X. W. (2024). Changes to Middle East and Southwest Asia compound drought and heat since 1999. *Journal of Climate,* 37(1), 269-287. https://doi.org/10.1175/JCLI-D-23-0194.1

Horan, M. F., Kucharski, F., Johnson, N., & Ashfaq, M. (2024). Winter precipitation predictability in Central Southwest Asia and its representation in seasonal forecast systems. *npj Climate and Atmospheric Science,* 7(1), 80. https://doi.org/10.1038/s41612-024-00594-5

Goudarzi, M., Ahmadi, H., & Hosseini, S. A. (2017). Examination of relationship between teleconnection indexes on temperature and precipitation components (Case Study: Karaj Synoptic Stations). *Iranian journal of Ecohydrology,* 4(3), 1-25. https://doi.org/10.22059/ije.2017.62414

Jolliffe, I. T., & Cadima, J. (2016). Principal component analysis: A review and recent developments. *Philosophical Transactions of the Royal Society A,* 374(2065), 20150202. https://doi.org/10.1098/rsta.2015.0202

Kalimeris, A., Ranieri, E., Founda, D., & Nor rant, C. (2017). Variability modes of precipitation along a Central Mediterranean area and their relations with ENSO, NAO, and other climatic patterns. *Atmospheric Research,* 198, 56-80. https://doi.org/10.1016/j.atmosres.2017.07.031

Kang, M. J., Kim, H., & Son, S. W. (2024). QBO modulation of MJO teleconnections in the North Pacific: impact of preceding MJO phases. *npj Climate and Atmospheric Science,* 7(1), 12. https://doi.org/10.1038/s41612-024-00565-w

Lee, J. H., Julien, P. Y., & Lee, S. (2023). Teleconnection of ENSO extreme events and precipitation variability over the United States. *Journal of Hydrology,* 619, 129206. https://doi.org/10.1016/j.jhydrol.2023.129206

Liu, Y., Xiao, J., Li, X., & Li, Y. (2024). Critical soil moisture detection and water-energy limit shift attribution using satellite-based water and carbon fluxes over China. *Hydrology and Earth System Sciences Discussions,* 2024, 1-30. https://doi.org/10.5194/hess-29-1241-2025

Lu, R., Hina, S., & Hong, X. (2020). Upper- and lower-tropospheric circulation anomalies associated with interannual variation of Pakistan rainfall during summer. *Advances in Atmospheric Sciences,* 37(11), 1179-1190. https://doi.org/10.1007/s00376-020-0137-0

Magnini, A., Lombardi, M., Ouarda, T. B., &Castellarin, A. (2024). AI-driven morphoclimatic regional frequency modelling of sub-daily rainfall-extremes. *Journal of Hydrology,* 631, 130808. https://doi.org/10.1016/j.jhydrol.2024.130808

Mehrvarz, Z., Saghafian, B., Raziei, T., &Hoghoughinia, K. (2025). An integrated PCA-Clustering model to extract homogeneous precipitation zones in Iran using monthly and seasonal patterns. *Modeling Earth Systems and Environment,* 11(4), 270. https://doi.org/10.1007/s40808-025-02455-3

Mwale, D., & Gan, T. Y. (2005). Wavelet analysis of variability, tele connectivity, and predictability of the September–November East African rainfall. *Journal of Applied Meteorology,* 44(2), 256–272. https://doi.org/10.1175/JAM2195.1

Nejad, M. T., Sharifi, L., & Lupo, A. R. (2022). The effect of northern hemisphere blocking systems on wet and dry periods in Iran under climate change conditions. https://doi.org/10.21203/rs.3.rs-2264505/v1

Pang, B., Scaife, A. A., Lu, R., Ren, R., &

Zhao, X. (2023). Interdecadal variations of the Scandinavian pattern. *Journal of Climate,* 36(10), 3275-3288. https://doi.org/10.1175/JCLI-D-22-0494.1

Richman, M. B. (1986). Rotation of principal components. *Journal of Climatology,* 6(3), 293–335. https://doi.org/10.1002/joc.3370060305

Rousi, E., Anagnostopoulou, C., Tolika, K., & Maheras, P. (2015). Representing teleconnection patterns over Europe: A comparison of SOM and PCA methods. A*tmospheric Research,* 152, 123–137. https://doi.org/10.1016/j.atmosres.2013.11.010

Rousta, I., Esmaeili Mahmoudabadi, A., Amini, P., Nikkhah, A., Olafsson, H., Krzyszczak, J., & Baranowski, P. (2023). Identification of Patterns and Relationships of Jet Stream Position with Flood-Prone Precipitation in Iran during 2006–2019. *Atmosphere,* 14(2), 351. https://doi.org/10.3390/atmos14020351

Saadatmoghadasi, A. (2025). Assessing the Influence of the Scandinavian Teleconnection Pattern on Precipitation and Relative Humidity Across Climatically Diverse Regions of Iran. *Iranian Journal of Soil and Water Research (Articles in Press).* https://doi.org/10.22059/ijswr.2025.398972.669983

Spuler, F. R., Kretschmer, M., Kovalchuk, Y., Balmaseda, M. A., & Shepherd, T. G. (2024). Identifying probabilistic weather regimes targeted to a local-scale impact variable. *Environmental Data Science, 3, e25.*https://doi.org/10.1017/eds.2024.29

Tao, X., Ben, M., Xuan, H. C. Y., &Arshaghi, A. (2025). A hybrid approach for regionalization of precipitation based on maximal discrete wavelet transform and growing neural gas network clustering. *Scientific Reports,* 15(1), 40611. https://doi.org/10.1038/s41598-025-24400-1

Vicente-Serrano, S. M., Tramblay, Y., Reig, F., González-Hidalgo, J. C., Beguería, S., Brunetti, M., ... & Potopová, V. (2025). High temporal variability not trend dominates Mediterranean precipitation. *Nature*, 639(8055), 658-666. https://doi.org/10.1038/s41586-024-08576-6

Wang, X., Liu, J., Tian, M., Huang, Y., Cao, T., & Zhang, X. (2009). A novel face feature extraction method based on two-dimensional principal component analysis and kernel discriminant analysis. *In 2009 International Conference on Information Management and Engineering*. IEEE. https://doi.org/10.1109/ICIME.2009.130

Yue, Y., & Wang, S. (2017). Kernel principal component analysis based on semisupervised dimensionality reduction and its application on protein subnuclear localization. *In 2017 10th International Congress on Image and Signal Processing, Biomedical Engineering and Informatics (CISPBMEI).* IEEE. https://doi.org/10.1109/CISP-BMEI.2017.8302284

Zilibotti, N., Wernli, H., & Schemm, S. (2025). A new look at the jet-storm track relationship in the North Pacific and North Atlantic. *EGUsphere, 2025, 1-32.* https://doi.org/10.5194/egusphere-2025-3605

Zittis, G. (2018). Observed rainfall trends and precipitation uncertainty in the vicinity of the Mediterranean, Middle East and North Africa. *Theoretical and applied climatology,* 134(3), 1207-1230. https://doi.org/10.1007/s00704-017-2333-0